Output-Feedback Finite-Time Safety-Critical Coordinated Control of Path-Guided Marine Surface Vehicles Based on Neurodynamic Optimization

Wentao Wu, *Student Member, IEEE*, Yibo Zhang, *Member, IEEE*, Weidong Zhang, *Senior Member, IEEE*, and Wei Xie, *Member, IEEE*

***Abstract*—In the presence of static and moving obstacles, this article investigates an output-feedback finite-time safety-critical coordinated control method of multiple under-actuated marine surface vehicles (MSVs) subject to velocity and input constraints. Specifically, based on robust exact differentiators, a finite-time state observer (FTSO) is first developed to recover the unavailable velocities while estimating the total disturbances containing model uncertainties and environmental disturbances. Next, with the aid of estimated velocities from FTSO, a nominal finite-time guidance law is designed for achieving the distributed formation of MSVs at the kinematic level. By the forward invariance principle, finite-time control barrier functions (FTCBFs) are used to construct the collision-free velocity sets for the multi-MSV system. To unify the control and safety objectives, quadratic optimization problems are formulated under collision-free velocity sets and velocity constraints. To facilitate real-time implementations, one-layer recurrent neural networks are employed to solve the quadratic optimization problem. Then, a nominal finite-time control law based on FTSO is presented at the kinetic level. The optimal control laws are solved within the input constraints. All error signals of the closed-loop system are proved to be uniformly ultimately bounded, and the distributed formation of multiple MSVs is ensured to be safe. Simulation results are provided to demonstrate the effectiveness and superiority of the proposed FTCBF-based method.**

***Index Terms*—Finite-time control barrier function (FTCBF), finite-time state observer (FTSO), neurodynamic optimization, safety-critical control, under-actuated marine surface vehicles (MSVs).**

Manuscript received 9 August 2022; accepted 3 September 2022. Date of publication 22 September 2022; date of current version 16 February 2023. This work was supported in part by the Shanghai Science and Technology Program under Grant 22015810300 and Grant 19510745200; in part by the Hainan Province Science and Technology Special Fund under Grant ZDYF2021GXJS041; in part by the National Natural Science Foundation of China under Grant U2141234 and Grant 52201369; in part by the Hainan Special Ph.D. Scientific Research Foundation of Sanya Yazhou Bay Science and Technology City under Grant HSPHDSRF-2022-01-007; and in part by the Shanghai Sailing Program under Grant 22YF1420400. This article was recommended by Associate Editor M. J. Er. *(Corresponding author: Weidong Zhang.)*

Wentao Wu is with the Department of Automation, Shanghai Jiao Tong University, Shanghai 200240, China, and also with SJTU Sanya Yazhou Bay Institute of Deepsea Science and Technology, Sanya 572024, Hainan, China (e-mail: wentao-wu@sjtu.edu.cn).

Yibo Zhang and Wei Xie are with the Department of Automation, Shanghai Jiao Tong University, Shanghai 200240, China (e-mail: zhang297@sjtu.edu.cn; weixie@sjtu.edu.cn).

Weidong Zhang is with the Department of Automation, Shanghai Jiao Tong University, Shanghai 200240, China (e-mail: wdzhang@sjtu.edu.cn).

Color versions of one or more figures in this article are available at https://doi.org/10.1109/TSMC.2022.3205637.

Digital Object Identifier 10.1109/TSMC.2022.3205637

I. Introduction

OVER the past few decades, formation control of marine surface vehicles (MSVs) has attracted ever-increasing attention from both research and industrial communities due to its widespread promising application, such as marine geodesy and cartography, marine search and rescue, and offshore installation protection, to name a few [1], [2], [3], [4]. The multi-MSV formation is more efficient and reliable to than a single vehicle for missions. However, in addition to static and dynamic obstacles, a large group of MSVs also poses a huge challenge to formation safety [5], [6], [7].

In the complex and dynamic marine environment, the safe operation of marine vehicles is of great importance to mission execution owing to no helmsman supervision. In order to guarantee the formation safety of multiple MSVs, there have existed some relative works based on predefined performance techniques [8], [9], [10], [11], artificial potential functions [12], [13], [14], [15], model predictive control [16]. Specifically, in [8], a transformed error surface is devised to achieve the predefined formation, connectivity preservation, and collision avoidance without switching the pattern. In [9], a robust leader-follower formation controller is designed for under-actuated MSVs while guaranteeing the connectivity and collision avoidance. In [10], a decentralized performance-guaranteed leader–follower formation controller is designed for full-actuated MSVs without collisions from their leaders. In addition to the desired transient performance and collision avoidance, [11] considers the connectivity maintenance between the follower MSV and its leader. Peng *et al.* [14] presented an output-feedback flocking control method, which is capable of avoiding collisions among neighboring MSVs. And the similar result can be achieved by the model predictive control strategy in [16]. In [12], a distributed time-varying formation controller is developed for under-actuated MSVs encountering static obstacles. In [13], a nonlinear extended state observer (ESO) is designed to achieve the collision-free cooperative formation of MSVs without measurable velocities. In [15], a finite-time containment maneuvering control method is designed for under-actuated marine vehicles guided by

multiple parameterized paths. In [17], a p-times differentiable step function is introduced into a synchronization tracking controller for guaranteeing no collisions among surface vehicles. In [18], a distributed robust formation control strategy based on the limit cycle is proposed for a heterogeneous formation of MSVs by using persistent excitation. In [19], an adaptive fuzzy event-triggered control method based on COLREGs is developed for surface vehicles encountering the obstructive ones in head-on, overtaking, and crossing situations. It is found that most collision-free methods in [8], [9], [10], [11], [12], [13], [14], [15], [16], [17], [18], and [19] are designed for only one type of obstacle, i.e., the obstructive vessel, the static, or dynamic obstacle. However, three types of obstacles may exist simultaneously in the unknown marine environment. Second, it is also worthy of attention to minimizing the loss of tracking performance while avoiding obstacles. In addition, upper and lower bounds of the velocity and control inputs of marine vehicles are critically physical variables in safe navigation.

Motivated by the above observations, we propose an output-feedback finite-time safety-critical coordinated control method for uncertain under-actuated MSVs with velocity and input constraints subject to static and moving obstacles. First, to recover the unavailable velocities and total disturbances, a finite-time state observer (FTSO) is developed based on robust exact differentiator (RED). Next, in the guidance loop, a nominal finite-time distributed guidance law is devised by using the recovered velocities. To avoid collision, finite-time control barrier functions (FTCBFs) are used to construct the collision-free constraints by using the position information of MSVs. Then, a distributed quadratic optimization is formulated to unify velocity constraints and multiple collision-free constraints. To solve the real-time quadratic optimization, a one-layer recurrent neural network (RNN) is employed to calculate the optimal safety-critical guidance law. In the kinetic control loop, a nominal finite-time kinetic control law is developed, and an optimal control law is solved under input constraints. Finally, error signals of the closed-loop system are proved to be uniformly ultimately bounded, and the safety of multi-MSV system is also guaranteed. Comparison results show the effectiveness and superiority of the proposed method.

Compared with the existing results in [8], [9], [10], [11], [12], [13], [14], [15], [16], [17], [18], [19], [20], [21], [22], [23], [24], [25], [26], [27], [28], [29], [30], [31], [32], [33], and [34], the foremost features of the proposed method are summarized in the following threefold.

1) In contrast to collision-free strategies in [8], [9], [10], [11], [12], [13], [14], [15], [16], [17], [18], and [19], the proposed FTCBF-based coordinated control method can achieve the safety-critical formation of a group of under-actuated MSVs regardless of the static, moving obstacles, and neighboring MSVs. In addition, the optimal velocity signals solved by the neurodynamic optimization are capable of degrading the tracking performance less when the collision avoidance behavior occurs.
2) In contrast to the centralized/decentralized architecture in [8], [9], [10], [11], [17], [18], [19], [27], and [28], the proposed distributed coordinated control scheme is able to reduce the communication burden and has fault tolerance and scalability. Unlike the coordinated controllers in [8], [9], [10], [11], [12], [13], [14], [15], [16], [17], [18], [19], [20], [21], [22], [23], and [24], the proposed finite-time controller can achieve collision-free formation within finite time without violating the velocity and input constraints.
3) In contrast to the state-feedback control methods in [8], [9], [10], [11], [12], [18], [22], [25], [26], [29], and [30] with exact velocities measured by additional sensors, the FTSO-based control method can decline the hardware cost of formation system, especially with more individuals. Different from linear/nonlinear ESOs in [13], [14], [20], and [22] and neural network-based adaptive approximation in [19], [21], [31], and [32], the proposed RED-based FTSO has the faster convergence speed and fewer tuning coefficients.

The arrangement of this article is given as follows. Section II states the preliminaries and problem formulation. Section III designs the finite-time safety-critical formation controller. Section IV analyzes the stability and safety of the closed-loop system. Section V gives the simulation results. Section VI concludes this article.

The following notations are used throughout this article. $\mathbb{R}^+$, $\mathbb{R}^n$, and $\mathbb{R}^{n\times m}$ present a positive real set, an n-dimensional matrix set and an $n \times m$-dimensional matrix set, respectively. diag$\{\cdots\}$ is a block-diagonal matrix. $(\cdot)^{\mathrm{T}}$ represents a matrix transpose. $|\cdot|$ and $\|\cdot\|$ stand for the absolute value and the Euclidean norm, respectively. For a state variable $\boldsymbol{x} = [x_1, \ldots, x_n]^{\mathrm{T}} \in \mathbb{R}^n$ and a real number $a \in [0, 1)$, $\lceil \boldsymbol{x} \rfloor^a$ presents a power function expressed as $\lceil \boldsymbol{x} \rfloor^a = [|x_1|^a \mathrm{sign}(x_1), \ldots, |x_n|^a \mathrm{sign}(x_n)]^{\mathrm{T}}$, where sign$(\cdot)$ is a signum function.

II. Preliminaries and Problem Formulation

A. Graph Theory

Consider a network with M MSVs, $N - M$ virtual leaders, and one super leader. A graph $\mathcal{G} = \{\mathcal{V}, \mathcal{E}\}$ is used to describe the communication topology of the multi-MSV network. $\mathcal{V}$ is a node-set with $\mathcal{V} = \{\mathcal{V}^S, \mathcal{V}^L, \mathcal{V}^F\}$ being the sets of the super leader, virtual leaders, and MSVs. $\mathcal{E}$ represents an edge set $\mathcal{E} = \{(i, j) \in \mathcal{V} \times \mathcal{V}\}$, where (i, j) means that the node i can receive the information of node j. The neighborhood set $\mathcal{N}_i$ of node i is defined as $\mathcal{N}_i = \{\mathcal{N}_i^S, \mathcal{N}_i^L, \mathcal{N}_i^F\}$, where $\mathcal{N}_i^S = \{j \in \mathcal{V}^S | (i, j) \in \mathcal{E}\}$, $\mathcal{N}_i^L = \{j \in \mathcal{V}^L | (i, j) \in \mathcal{E}\}$ and $\mathcal{N}_i^F = \{j \in \mathcal{V}^F | (i, j) \in \mathcal{E}\}$. The sequences $(i, k), (k, m), \ldots, (n, j)$ are called a successive edge which indicates a directed path from node i to node j. An adjacent matrix $\mathcal{A} = [a_{ij}] \in \mathbb{R}^{N\times N}$ describes the links among nodes with $a_{ij} = 1$ for $(i, j) \in \mathcal{E}$ or $a_{ij} = 0$ for $(i, j) \notin \mathcal{E}$. The graph with $a_{ij} = a_{ji}$ is called an undirected graph. Define an in-degree matrix $\mathcal{D} = \mathrm{diag}\{d_i\} \in \mathbb{R}^{N\times N}$ with $d_i = \sum_{j=1}^{N} a_{ij}$. A Laplacian matrix $\mathcal{L} \in \mathbb{R}^{N\times N}$ satisfies $\mathcal{L} = \mathcal{D} - \mathcal{A}$.

B. Finite-Time Control Barrier Function

Consider a nonlinear affine control system as follows:

$$\dot{\boldsymbol{x}} = \boldsymbol{f}(\boldsymbol{x}) + \boldsymbol{g}(\boldsymbol{x})\boldsymbol{u} \tag{1}$$

where $\boldsymbol{x} \in \mathcal{D} \subset \mathbb{R}^n$ and $\boldsymbol{u} \in \mathbb{R}^m$ are the state and the control input, respectively. $\boldsymbol{f}(\boldsymbol{x}) \in \mathbb{R}^n$ and $\boldsymbol{g}(\boldsymbol{x}) \in \mathbb{R}^{n\times m}$ are locally Lipschitz continuous functions.

Definition 1 [35]: With a continuously differentiable function $h(\boldsymbol{x}) : \mathcal{D} \to \mathbb{R}$, a super level set $\mathcal{C} \subset \mathcal{D}$ for the system (1) is defined as follows:

$$\begin{aligned} \mathcal{C} &= \{\boldsymbol{x} \in \mathcal{D} : h(\boldsymbol{x}) \geq 0\} \\ \partial\mathcal{C} &= \{\boldsymbol{x} \in \mathcal{D} : h(\boldsymbol{x}) = 0\} \\ \text{Int}(\mathcal{C}) &= \{\boldsymbol{x} \in \mathcal{D} : h(\boldsymbol{x}) > 0\}. \end{aligned} \tag{2}$$

The set $\mathcal{C}$ is called a forward invariant set if $\boldsymbol{x}(t) \in \mathcal{C}\ \forall t \geq t_0$ for any $\boldsymbol{x}(t_0) \in \mathcal{C}$. The forward invariance of $\mathcal{C}$ also means that the system (1) is safe.

Definition 2 [36]: Given a system (1) and a safe set $\mathcal{C}$ defined by (2), a continuously differentiable function $h(\boldsymbol{x}) : \mathcal{D} \to \mathbb{R}$ is called an FTCBF defined on the set $\mathcal{C}$ if there exist constants $\beta \in [0, 1)$, $\varkappa \in \mathbb{R}^+$ such that, for all $\boldsymbol{x} \in \mathcal{D}$

$$\sup_{\boldsymbol{u}\in\mathbb{R}^m} \left[L_f h(\boldsymbol{x}) + L_g h(\boldsymbol{x})\boldsymbol{u} + \varkappa\lceil h(\boldsymbol{x})\rfloor^{\beta}\right] \geq 0. \tag{3}$$

Then, an admissible control input set with an FTCBF $h(\boldsymbol{x})$ for the system (1) can be described as follows:

$$\mathcal{U}(\boldsymbol{x}) = \left\{\boldsymbol{u} \in \mathbb{R}^m : L_f h(\boldsymbol{x}) + L_g h(\boldsymbol{x})\boldsymbol{u} + \varkappa\lceil h(\boldsymbol{x})\rfloor^{\beta} \geq 0\right\} \tag{4}$$

where $L_f h(\boldsymbol{x})$ and $L_g h(\boldsymbol{x})$ are the Lie derivatives of $h(\boldsymbol{x})$ along the system (1), which satisfying

$$L_f h(\boldsymbol{x}) + L_g h(\boldsymbol{x})\boldsymbol{u} = \frac{\partial h(\boldsymbol{x})}{\partial \boldsymbol{x}}(\boldsymbol{f}(\boldsymbol{x}) + \boldsymbol{g}(\boldsymbol{x})\boldsymbol{u}).$$

Lemma 1 [36]: Given a safe set $\mathcal{C} \subset \mathbb{R}^n$ defined by (2) with the corresponding FTCBF $h(\boldsymbol{x})$, $\beta \in [0, 1)$ and $\varkappa \in \mathbb{R}^+$, any continuous controller $\boldsymbol{u} : \mathcal{D} \to \mathbb{R}^m$ such that $\boldsymbol{u} \in \mathcal{U}(\boldsymbol{x})$ for the system (1) renders that the set $\mathcal{C}$ is forward invariant. Supposed the initial state $\boldsymbol{x}(t_0) \in \mathcal{D}\backslash\mathcal{C}$, any continuous controller $\boldsymbol{u} \in \mathcal{U}(\boldsymbol{x})$ for the system (1) will drive the state $\boldsymbol{x}(t)$ to the set $\mathcal{C}$ in a finite time $T = |h(t_0)|^{1-\beta}/\varkappa(1-\beta)$.

C. Problem Formulation

Consider a path-guided coordinated control system containing of M MSVs and $N - M$ virtual leaders shown in Fig. 1. In the earth-fixed reference frame $X_E - Y_E$ and the vehicle-fixed reference frame $X_B - Y_B$, the model dynamics of the ith under-actuated MSV are presented as follows [37]:

$$\begin{cases} \dot{\boldsymbol{\eta}}_i = \boldsymbol{R}(\psi_i)\boldsymbol{v}_i, \quad i = 1, \ldots, M \\ \boldsymbol{M}_i\dot{\boldsymbol{v}}_i + \boldsymbol{C}_i\boldsymbol{v}_i + \boldsymbol{D}_i\boldsymbol{v}_i + \boldsymbol{g}_i = \boldsymbol{\tau}_i + \boldsymbol{\tau}_{i\omega} \end{cases} \tag{5}$$

where $\boldsymbol{\eta}_i = [\boldsymbol{p}_i^{\mathrm{T}}, \psi_i]^{\mathrm{T}} \in \mathbb{R}^3$ is the position and yaw angle vector with $\boldsymbol{p}_i = [x_i, y_i]^{\mathrm{T}}$; $\boldsymbol{v}_i = [u_i, v_i, r_i]^{\mathrm{T}} \in \mathbb{R}^3$ represents a surge, sway, and yaw velocity vector satisfying $u_{i\min} \leq u_i \leq u_{i\max}$, $v_{i\min} \leq v_i \leq v_{i\max}$, and $r_{i\min} \leq r_i \leq r_{i\max}$ with $u_{i\min}, v_{i\min}, r_{i\min}, u_{i\max}, v_{i\max}, r_{i\max}$ being some constants; $\boldsymbol{M}_i = \text{diag}\{m_i^u, m_i^v, m_i^r\}$ is an inertial mass matrix; $\boldsymbol{C}_i = -\boldsymbol{C}_i^{\mathrm{T}} \in \mathbb{R}^{3\times3}$ denotes a Coriolis/centripetal matrix; $\boldsymbol{D}_i \in \mathbb{R}^{3\times3}$ represents a damping matrix; $\boldsymbol{g}_i \in \mathbb{R}^3$ is the unmodeled hydrodynamics; For an under-actuated MSV, $\boldsymbol{\tau}_i = [\tau_i^u, 0, \tau_i^r]^{\mathrm{T}} \in \mathbb{R}^3$ is a naturally bounded control input satisfying $0 \leq \tau_i^u \leq \tau_{i\max}^u$ and $-\tau_{i\max}^r \leq \tau_i^r \leq \tau_{i\max}^r$ with $\tau_{i\max}^u$ and $\tau_{i\max}^r$ being positive constants; $\boldsymbol{\tau}_{i\omega} \in \mathbb{R}^3$ is the environmental disturbance from wind, wave, and current; $\boldsymbol{R}(\psi_i)$ is a rotation matrix satisfying $\boldsymbol{R}(\psi_i) = \text{diag}\{\boldsymbol{R}'(\psi_i), 1\}$ and $\dot{\boldsymbol{R}}(\psi_i) = r_i\boldsymbol{S}\boldsymbol{R}(\psi_i)$ with

$$\boldsymbol{R}'(\psi_i) = \begin{bmatrix} \cos(\psi_i) & -\sin(\psi_i) \\ \sin(\psi_i) & \cos(\psi_i) \end{bmatrix} \text{ and } \boldsymbol{S} = \begin{bmatrix} 0 & -1 & 0 \\ 1 & 0 & 0 \\ 0 & 0 & 0 \end{bmatrix}.$$

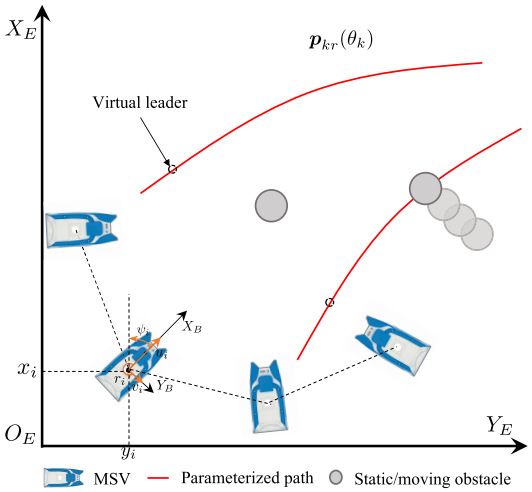

Fig. 1. Path-guided cooperative formation of multiple MSVs subject to static/dynamic obstacles.

Since three freedom degrees of under-actuated MSVs (5) cannot be controlled alone, it is extremely challenging to achieve the distributed collision-free formation. Then, the vehicle model (5) is transformed into an earth-fixed model as follows:

$$\begin{cases} \dot{\boldsymbol{p}}_i = \boldsymbol{q}_i & \text{(6a)} \\ \dot{\boldsymbol{q}}_i = \boldsymbol{\zeta}_{ib}^q + \boldsymbol{\tau}_{ib}^q & \text{(6b)} \\ \dot{\psi}_i = r_i & \text{(6c)} \\ \dot{r}_i = \zeta_{ib}^r + \tau_{ib}^r & \text{(6d)} \end{cases}$$

where $\boldsymbol{q}_i = \boldsymbol{R}'(\psi_i)[u_i, v_i]^{\mathrm{T}} = [q_i^x, q_i^y]^{\mathrm{T}} \in \mathbb{R}^2$ is the earth-fixed velocity; $\boldsymbol{\tau}_{ib}^q \in \mathbb{R}^2$ and $\tau_{ib}^r \in \mathbb{R}$ are the earth-fixed nominal control inputs satisfying $\boldsymbol{\tau}_{ib} = [\boldsymbol{\tau}_{ib}^{qT}, \tau_{ib}^r]^{\mathrm{T}} = \boldsymbol{R}(\psi_i)\boldsymbol{M}_i^{-1}\boldsymbol{\tau}_i$; $\boldsymbol{\zeta}_{ib}$ represents the earth-fixed total disturbances with $\boldsymbol{\zeta}_{ib} = [(\boldsymbol{\zeta}_{ib}^q)^{\mathrm{T}}, \zeta_{ib}^r]^{\mathrm{T}} = r_i\boldsymbol{S}\boldsymbol{R}(\psi_i)\boldsymbol{v}_i + \boldsymbol{R}(\psi_i)\boldsymbol{M}_i^{-1}(-\boldsymbol{C}_i\boldsymbol{v}_i - \boldsymbol{D}_i\boldsymbol{v}_i - \boldsymbol{g}_i + \boldsymbol{\tau}_{i\omega})$, where $\boldsymbol{\zeta}_{ib}^q = [\zeta_{ib}^x, \zeta_{ib}^y]^{\mathrm{T}}$. In addition, one has

$$\begin{cases} \|\boldsymbol{q}_i\| \leq \sqrt{u_{i\max}^2 + v_{i\max}^2}, \text{ and } |r_i| \leq r_{i\max} & \text{(7a)} \\ \|\boldsymbol{\tau}_{ib}^q\| \leq \tau_{i\max}^u/m_i^u, \text{ and } |\tau_{ib}^r| \leq \tau_{i\max}^r/m_i^r. & \text{(7b)} \end{cases}$$

In the path-guided coordinated control problem, multiple MSVs are driven to track the convex hulls spanned by MSVs and virtual leaders, which move along the predefined parameterized paths $\boldsymbol{p}_{kr}(\theta_k) = [x_{kr}(\theta_k), y_{kr}(\theta_k)]^{\mathrm{T}} \in \mathbb{R}^2, k = M + 1, \ldots, N$ with $\theta_k \in \mathbb{R}$ being a path variable. It is assumed that $\boldsymbol{p}_{kr}(\theta_k)$ and its partial derivative $\boldsymbol{p}_{kr}^{\theta} = \partial\boldsymbol{p}_{kr}(\theta_k)/\partial\theta_k$ are bounded. For the kth virtual leader, the parameter θ_k is updated by

$$\dot{\theta}_k = \upsilon_s - \chi_k \tag{8}$$

where $\upsilon_s \in \mathbb{R}$ is a predefined update speed. χ_k denotes a coordination error to be designed later. For the super leader, labeled as 0, with the dynamics $\dot{\theta}_0 = \upsilon_s$, it moves with a constant velocity υ_s.

To achieve the distributed coordinated formation, the virtual leaders and MSVs need to deliver self-information to their neighbors via the network/sensor. To describe the communication relationships, a graph $\mathcal{G}$ is used, and the corresponding Laplacian matrix $\mathcal{L} \in \mathbb{R}^{N\times N}$ is defined as

$$\mathcal{L} = \begin{bmatrix} \boldsymbol{L}_1 & \boldsymbol{L}_2 \\ \boldsymbol{L}_2^{\mathrm{T}} & \boldsymbol{L}_0 \end{bmatrix} \tag{9}$$

where $\boldsymbol{L}_0 \in \mathbb{R}^{(N-M)\times(N-M)}$, $\boldsymbol{L}_1 \in \mathbb{R}^{M\times M}$, and $\boldsymbol{L}_2 \in \mathbb{R}^{M\times(N-M)}$ reflect the information exchanges among virtual leaders, among MSVs, and between virtual leaders and MSVs, respectively.

The objective of this article is to devise an output-feedback finite-time safety-critical coordinated control method for path-guided multiple under-actuated MSVs with velocity/input constraints subject to static and moving obstacles. Then, the following objectives need to be satisfied.

1) Geometric Objective: Drive each MSV to track the corresponding convex hull spanned by virtual leaders within finite time, such that

$$\left\| \boldsymbol{p}_i(t) - \sum_{k\in\mathcal{N}_i^L} \alpha_k \boldsymbol{p}_{kr}(\theta_k) \right\| \le \delta_i \tag{10}$$

where $i = 1, \ldots, M$ and $\delta_i \in \mathbb{R}^+$. α_k is a positive constant with $\sum_{k=M+1}^{N} \alpha_k = 1$.

2) Dynamic Objective: Drive each virtual leader to complete the following tasks.

1) *Velocity Task:* The dynamics $\dot{\theta}_k$ converges to the predefined update velocity in finite time, such that

$$|\dot{\theta}_k - \upsilon_s| \le \delta_{k1} \tag{11}$$

where $k = M+1, \ldots, N$ and $\delta_{k1} \in \mathbb{R}^+$.

2) *Phase Task:* The path parameter θ_k converges to the parameter of the super leader with the predefined deviation Θ_k, such that

$$|\theta_k - \theta_0 - \Theta_k| \le \delta_{k2} \tag{12}$$

where $k = M+1, \ldots, N$ and $\delta_{k2} \in \mathbb{R}^+$.

3) Safety Objective: Ensure each MSV in the safe region.

1) *Inter-MSV Collision Avoidance:* The distance among each MSV and its neighboring MSVs meets

$$\|\boldsymbol{p}_i - \boldsymbol{p}_j\| \ge D_s \in \mathbb{R}^+ \tag{13}$$

where $i = 1, \ldots, M, j \in \mathcal{V}_i^F \backslash \{i\}$. D_s presents the extreme collision-free radius.

2) *Obstacle Collision Avoidance:* The distance between each MSV and the static/moving obstacles meets

$$\lim_{t\to T} \|\boldsymbol{p}_i - \boldsymbol{p}_o\| \ge D_o + \rho_o \tag{14}$$

where $i = 1, \ldots, M$ and $o = 1, \ldots, N_o$. $D_o \in \mathbb{R}^+$ and $\rho_o \in \mathbb{R}^+$ denote the minimum safe distance and the radius of the oth obstacle.

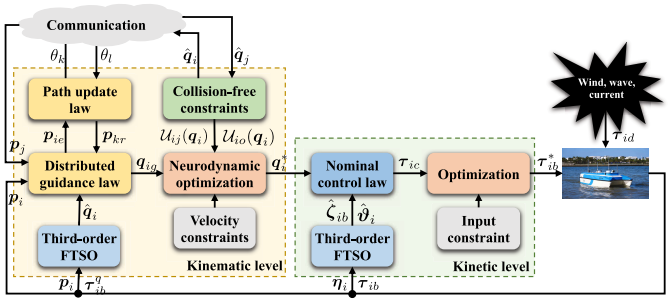

Fig. 2. Block diagram of the proposed finite-time safety-critical formation controller.

The following assumptions are needed in this article.

Assumption 1: The graph $\mathcal{G}$ is undirected and has a spanning tree with a super leader as a root node.

Assumption 2 [38]: The time derivative of $\boldsymbol{\zeta}_{ib}$ is bounded and satisfied with $\|\dot{\boldsymbol{\zeta}}_{ib}\| \le \bar{\zeta}_{ib} \in \mathbb{R}^+$.

Remark 1: This article studies a distributed coordinated control of multiple MSVs under an undirected communication topology. To achieve the distributed formation guided by a super leader, it is natural to have a spanning tree with the super leader as a root node. Thus, Assumption 1 is reasonable, and similar assumptions can be found in [31] and [39]. For a practical marine vehicle, the velocity-involved terms $\boldsymbol{\zeta}_{ib}$ and $\dot{\boldsymbol{\zeta}}_{ib}$ are naturally bounded due to the limited energy and constrained actuators. Besides, the environmental disturbances from wind, wave, and current are also bounded. Thereby, Assumption 2 is reasonable for MSVs. Similar assumption can be found in [13], [38], and [40].

III. Controller Design

This section proposes an FTCBF-based output-feedback finite-time safety-critical coordinated control method for path-guided under-actuated MSVs with the velocity and input constraints subject to static/moving obstacles. The block diagram of the proposed method is shown in Fig. 2.

A. Finite-Time State Observer

The velocity is a vital maritime signal for marine vehicles moving on the sea. When the velocities are unavailable, it becomes very challenging for the motion control of MSVs, especially for the collision-free formation. According to [39] and [41], ESO is an efficient tool to estimate the unknown state and disturbances, simultaneously. To improve the convergence speed and estimation accuracy, an RED-based FTSO is developed to estimate $\boldsymbol{q}_i$, r_i, and $\boldsymbol{\zeta}_{ib}$ as follows:

$$\begin{cases} \dot{\hat{\boldsymbol{\eta}}}_i = -\mu_{i1} L_i^{\frac{1}{3}} \left\lceil \hat{\boldsymbol{\eta}}_i - \boldsymbol{\eta}_i \right\rfloor^{\frac{2}{3}} + \hat{\boldsymbol{\vartheta}}_i \\ \dot{\hat{\boldsymbol{\vartheta}}}_i = -\mu_{i2} L_i^{\frac{2}{3}} \left\lceil \hat{\boldsymbol{\eta}}_i - \boldsymbol{\eta}_i \right\rfloor^{\frac{1}{3}} + \hat{\boldsymbol{\zeta}}_{ib} + \boldsymbol{\tau}_{ib} \\ \dot{\hat{\boldsymbol{\zeta}}}_{ib} = -\mu_{i3} L_i \left\lceil \hat{\boldsymbol{\eta}}_i - \boldsymbol{\eta}_i \right\rfloor^{0} \end{cases} \tag{15}$$

where $\hat{\boldsymbol{\eta}}_i = [\hat{\boldsymbol{p}}_i^{\mathrm{T}}, \hat{\psi}_i]^{\mathrm{T}}$, $\hat{\boldsymbol{\vartheta}}_i = [\hat{\boldsymbol{q}}_i^{\mathrm{T}}, \hat{r}_i]^{\mathrm{T}}$, and $\hat{\boldsymbol{\zeta}}_{ib} = [(\hat{\boldsymbol{\zeta}}_{ib}^{q})^{\mathrm{T}}, \hat{\zeta}_{ib}^{r}]^{\mathrm{T}}$ present the estimated values of $\boldsymbol{\eta}_i$, $\boldsymbol{\vartheta}_i$, and $\boldsymbol{\zeta}_{ib}$ with $\boldsymbol{\vartheta}_i = [\boldsymbol{q}_i^{\mathrm{T}}, r_i]^{\mathrm{T}}$, respectively. μ_{i1}, μ_{i2}, $\mu_{i3} \in \mathbb{R}^+$ are the observer coefficients. $L_i \in \mathbb{R}^+$ denotes a scaling factor.

Apply the variable changes $\tilde{\boldsymbol{\eta}}_i = L_i\boldsymbol{E}_{i1}$, $\tilde{\boldsymbol{\vartheta}}_i = L_i\boldsymbol{E}_{i2}$, and $\tilde{\boldsymbol{\zeta}}_{ib} = L_i\boldsymbol{E}_{i3}$ with $\tilde{\boldsymbol{\eta}}_i = \hat{\boldsymbol{\eta}}_i - \boldsymbol{\eta}_i$, $\tilde{\boldsymbol{\vartheta}}_i = \hat{\boldsymbol{\vartheta}}_i - \boldsymbol{\vartheta}_i$, and $\tilde{\boldsymbol{\zeta}}_{ib} = \hat{\boldsymbol{\zeta}}_{ib} - \boldsymbol{\zeta}_{ib}$. Using (7) and (15), the dynamics of $\boldsymbol{E}_{i1}$, $\boldsymbol{E}_{i2}$, and $\boldsymbol{E}_{i3}$ are deduced as follows:

$$\begin{cases} \dot{\boldsymbol{E}}_{i1} = -\mu_{i1}\lceil \boldsymbol{E}_{i1}\rfloor^{\frac{2}{3}} + \boldsymbol{E}_{i2} \\ \dot{\boldsymbol{E}}_{i2} = -\mu_{i2}\lceil \boldsymbol{E}_{i1}\rfloor^{\frac{1}{3}} + \boldsymbol{E}_{i3} \\ \dot{\boldsymbol{E}}_{i3} = -\mu_{i3}\lceil \boldsymbol{E}_{i1}\rfloor^{0} - \dot{\boldsymbol{\zeta}}_{ib}/L_i. \end{cases} \tag{16}$$

According to the stability conclusion in [42] and [43], the error dynamics of RED-based FTSO in (16) is finite-time stable if Assumption 2 is satisfied. The estimated errors $\tilde{\boldsymbol{\eta}}_i$, $\tilde{\boldsymbol{\vartheta}}_i$, and $\tilde{\boldsymbol{\zeta}}_{ib}$ can converge to small neighborhoods of the origin within finite time and satisfy $\|\tilde{\boldsymbol{\eta}}_i\| \le \bar{\eta}_i \in \mathbb{R}^+$ and $\|\tilde{\boldsymbol{\vartheta}}_i\| \le \bar{\vartheta}_i \in \mathbb{R}^+$.

B. Distributed Finite-Time Safety-Critical Guidance Law

In this section, a distributed finite-time safety-critical guidance law is developed for multiple under-actuated MSVs based on the FTCBF and neurodynamic optimization technique. Then, a finite-time path update law is designed for multiple virtual leaders.

First, a distributed kinematic tracking error $\boldsymbol{p}_{ie}$ is defined as follows:

$$\boldsymbol{p}_{ie} = \sum_{j\in\mathcal{N}_i^F} a_{ij}(\boldsymbol{p}_i - \boldsymbol{p}_j) + \sum_{k\in\mathcal{N}_i^L} a_{ik}(\boldsymbol{p}_i - \boldsymbol{p}_{kr}(\theta_k)). \tag{17}$$

By the submodel (6a) and parameter dynamics (8), it yields the derivative of $\boldsymbol{p}_{ie}$ as follows:

$$\dot{\boldsymbol{p}}_{ie} = d_i\boldsymbol{q}_i - \sum_{j\in\mathcal{N}_i^F} a_{ij}\boldsymbol{q}_j - \sum_{k\in\mathcal{N}_i^L} a_{ik}\dot{\boldsymbol{p}}_{kr}(\theta_k) \tag{18}$$

where $d_i = \sum_{j=1}^{N} a_{ij}$ and $\dot{\boldsymbol{p}}_{kr}(\theta_k) = \boldsymbol{p}_{kr}^{\theta}(\upsilon_s - \chi_k)$.

To stabilize the error dynamics (18), a nominal finite-time guidance law is proposed as follows:

$$\boldsymbol{q}_{ig} = \frac{1}{d_i}\left(-\mu_{ig}^{q}\lceil \boldsymbol{p}_{ie}\rfloor^{\frac{1}{2}} + \sum_{j\in\mathcal{N}_i^F} a_{ij}\hat{\boldsymbol{q}}_j + \sum_{k\in\mathcal{N}_i^L} a_{ik}\boldsymbol{p}_{kr}^{\theta}\upsilon_s\right) \tag{19}$$

where $\mu_{ig}^{q} \in \mathbb{R}^+$ is a control gain.

To coordinate the virtual leaders, the variable χ_k for the kth virtual leader is presented as follows:

$$\chi_k = -\mu_{kg}^{\chi}\lceil e_k\rfloor^{\frac{1}{2}} \tag{20}$$

where $\mu_{kg}^{\chi} \in \mathbb{R}^+$ is a tuning gain. $e_k = \sum_{i\in\mathcal{N}_k^F} a_{ki}\boldsymbol{p}_{kr}^{\theta T}\boldsymbol{p}_{ie} - \theta_{ke}$ with $\theta_{ke} = \sum_{l\in\mathcal{N}_k^L} a_{kl}(\theta_k - \theta_l - \Theta_{kl})$, where $\Theta_{kl} = \Theta_k - \Theta_l$, $k = M+1,\ldots,N$, $k \ne l$.

Define a global path coordination error as $\bar{\theta}_{ke} = \theta_k - \theta_0$. Then, it takes the derivative of $\bar{\theta}_{ke}$ along (8) as follows:

$$\dot{\bar{\theta}}_{ke} = -\chi_k. \tag{21}$$

Let $\bar{\boldsymbol{\theta}}_e = [\bar{\theta}_{(M+1)e},\ldots,\bar{\theta}_{Ne}]^{\mathrm{T}} \in \mathbb{R}^{N-M}$ and $\boldsymbol{\theta}_e = [\theta_{(M+1)e},\ldots,\theta_{Ne}]^{\mathrm{T}} \in \mathbb{R}^{N-M}$ be a global and local path coordination error vectors, respectively. Then, it yields that $\boldsymbol{\theta}_e = \mathcal{H}\bar{\boldsymbol{\theta}}_e$, where $\mathcal{H} = \mathcal{L}_0 + \mathcal{A}_0$ with $\mathcal{A}_0 = \mathrm{diag}\{a_{(M+1)0},\ldots,a_{N0}\}$ being a leader adjacency matrix.

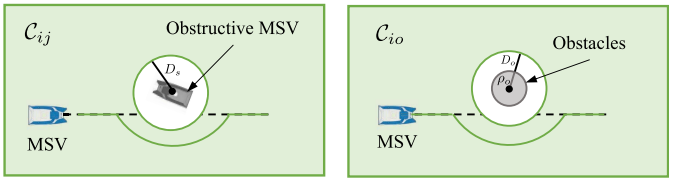

Fig. 3. Collision-free sets based on FTCBF.

Substituting (19) into (18), the error dynamics of $\boldsymbol{p}_{ie}$ and $\bar{\theta}_{ke}$ are deduced as follows:

$$\begin{cases} \dot{\boldsymbol{p}}_{ie} = -\mu_{ig}^{q}\lceil \boldsymbol{p}_{ie}\rfloor^{\frac{1}{2}} + d_i\hat{\boldsymbol{q}}_{ie} - d_i\tilde{\boldsymbol{q}}_i \\ \qquad + \sum_{j\in\mathcal{N}_i^F} a_{ij}\tilde{\boldsymbol{q}}_j - \sum_{k\in\mathcal{N}_i^L} a_{ik}\boldsymbol{p}_{kr}^{\theta}\chi_k \\ \dot{\bar{\theta}}_{ke} = -\chi_k \end{cases} \tag{22}$$

where $\hat{\boldsymbol{q}}_{ie} = \hat{\boldsymbol{q}}_i - \boldsymbol{q}_{ig}$.

To guarantee the formation safety of under-actuated MSVs subject to static/moving obstacles, a safety-critical guidance signal is needed. Motivated by the safe set in [35] and [36], the objectives (13) and (14) are converted into ensuring the forward invariance of the corresponding safe sets, respectively. Then, the collision-free sets $\mathcal{C}_{ij}$ and $\mathcal{C}_{io}$ based on the position information are constructed as follows:

$$\begin{cases} \mathcal{C}_{ij} = \{\boldsymbol{p}_i \in \mathbb{R}^2 : h_{ij}(\boldsymbol{p}_i) \ge 0\} \\ \mathcal{C}_{io} = \{\boldsymbol{p}_i \in \mathbb{R}^2 : h_{io}(\boldsymbol{p}_i) \ge 0\} \end{cases} \tag{23}$$

where $h_{ij}(\boldsymbol{p}_i)$ and $h_{io}(\boldsymbol{p}_i)$ are FTCBFs to design later. Fig. 3 is used to further illustrate the principle of the collision avoidance. In the left picture, MSV will always stay in the safe zone, i.e., $\boldsymbol{p}_i(t) \in \mathcal{C}_{ij}$, $t > t_0$ if the initial state satisfies $\boldsymbol{p}_i(t_0) \in \mathcal{C}_{ij}$. When $\boldsymbol{p}_i(t_0) \notin \mathcal{C}_{ij}$, the safety-critical guidance signal with the FTCBF $h_{ij}(\boldsymbol{p}_i)$ drives the MSV to the safe zone within finite time. It means that the MSV can avoid its neighboring MSV, i.e., the ith MSV is safe. The right picture is similar to the left one.

Based on the safety objective (13), the FTCBF $h_{ij}(\boldsymbol{p}_i)$ is constructed to avoid collision among neighboring MSVs

$$h_{ij}(\boldsymbol{p}_i) = \|\boldsymbol{p}_i - \boldsymbol{p}_j\|^2 - D_s^2 \tag{24}$$

where $i = 1,\ldots,M, j \in \mathcal{V}^F\backslash\{i\}$. By using (4), (6a), and (24), a collision-free velocity set $\mathcal{U}_{ij}(\boldsymbol{q}_i)$ is presented as follows:

$$\mathcal{U}_{ij}(\boldsymbol{q}_i) := \Big\{\boldsymbol{q}_i \in \mathbb{R}^2 : L_{f_i}h_{ij}(\boldsymbol{p}_i) + L_{\boldsymbol{g}_i}h_{ij}(\boldsymbol{p}_i)\boldsymbol{q}_i + \varkappa_{ij}\lceil h_{ij}(\boldsymbol{p}_i)\rfloor^{\beta_{ij}} \ge 0\Big\} \tag{25}$$

where $L_{f_i}h_{ij}(\boldsymbol{p}_i)$ and $L_{\boldsymbol{g}_i}h_{ij}(\boldsymbol{p}_i)$ represent the Lie derivatives of $h_{ij}(\boldsymbol{p}_i)$ along the dynamics (6a). $\varkappa_{ij} \in \mathbb{R}^+$ and $\beta_{ij} \in [0,1)$ are designed constants.

Similarly, based on the safety objective (14), a collision-free set $\mathcal{U}_{io}(\boldsymbol{q}_i)$ is developed to avoid the static/moving obstacles

$$\mathcal{U}_{io}(\boldsymbol{q}_i) := \Big\{\boldsymbol{q}_i \in \mathbb{R}^2 : L_{f_i}h_{io}(\boldsymbol{p}_i) + L_{\boldsymbol{g}_i}h_{io}(\boldsymbol{p}_i)\boldsymbol{q}_i + \varkappa_{io}\lceil h_{io}(\boldsymbol{p}_i)\rfloor^{\beta_{io}} \ge 0\Big\} \tag{26}$$

where $h_{io}(\boldsymbol{p}_i) = \|\boldsymbol{p}_i - \boldsymbol{p}_o\|^2 - (D_s + \rho_o)^2$, $i = 1,\ldots,M$, $o = 1,\ldots,N_o$. $L_{f_i}h_{io}(\boldsymbol{p}_i)$ and $L_{\boldsymbol{g}_i}h_{io}(\boldsymbol{p}_i)$ are Lie derivatives of

$h_{io}(\boldsymbol{p}_i)$ along (6a). $\varkappa_{io} \in \mathbb{R}^+$ and $\beta_{io} \in [0, 1)$ are the designed constants.

In order to minimize the impact on the tracking performance of the multi-MSV, a quadratic optimization is formulated to unify the collision-free constraints $\mathcal{U}_{ij}(\boldsymbol{q}_i)$ and $\mathcal{U}_{io}(\boldsymbol{q}_i)$ and the velocity constraint (7a). Then, the optimal velocity signal $\boldsymbol{q}_i^*$ is solved as follows:

$$\begin{aligned} \boldsymbol{q}_i^* = \underset{\boldsymbol{q}_i \in \mathbb{R}^2}{\operatorname{argmin}} \ & J_i^q(\boldsymbol{q}_i) = \|\boldsymbol{q}_i - \boldsymbol{q}_{ig}\|^2 \\ \text{s.t.} \ & \boldsymbol{q}_i \in \mathcal{U}_{ij}(\boldsymbol{q}_i) \\ & \boldsymbol{q}_i \in \mathcal{U}_{io}(\boldsymbol{q}_i) \\ & \|\boldsymbol{q}_i\| \le \sqrt{u_{i\max}^2 + v_{i\max}^2} \end{aligned} \tag{27}$$

with $i = 1, \ldots, M, j \in \mathcal{V}^F \backslash \{i\}$ and $o = 1, \ldots, N_o$.

The quadratic optimization problem in (27) is a typical multiconstraint optimization problem, which is able to be solved by the neurodynamic optimization technique [44]. To enhance real-time implementations, the following one-layer RNN is used to solve (27) as follows:

$$\epsilon_i \dot{\boldsymbol{q}}_i = -\nabla J_i^q(\boldsymbol{q}_i) - \frac{1}{\iota_i} \sum_{k=1}^{d_i+N_o+1} \partial \max\{0, \varsigma_{ik}(\boldsymbol{q}_i)\} \tag{28}$$

where $\epsilon_i \in \mathbb{R}^+$ and $\iota_i \in \mathbb{R}^+$ present a convergent time constant and a penalty parameter, respectively. $\varsigma_{ik}(\boldsymbol{q}_i) = -L_{\boldsymbol{g}_i} h_{ij}(\boldsymbol{p}_i)\boldsymbol{q}_i - L_{\boldsymbol{f}_i} h_{ij}(\boldsymbol{p}_i) - \varkappa_{ij} \lceil h_{ij}(\boldsymbol{p}_i) \rfloor^{\beta_{ij}}, k = 1, \ldots, d_i$, $\varsigma_{ik} = -L_{\boldsymbol{g}_i} h_{io}(\boldsymbol{p}_i)\boldsymbol{q}_i - L_{\boldsymbol{f}_i} h_{io}(\boldsymbol{p}_i) - \varkappa_{io} \lceil h_{io}(\boldsymbol{p}_i) \rfloor^{\beta_{io}}, k = d_i + 1, \ldots, d_i + N_o$, and $\varsigma_{i(d_i+N_o+1)} = \|\boldsymbol{q}_i\| - \bar{q}_i$. $\partial \max\{0, \varsigma_{ik}(\boldsymbol{q}_i)\}$ is an exact penalty function expressed as

$$\partial \max\{0, \varsigma_{ik}(\boldsymbol{q}_i)\} = \begin{cases} \nabla \varsigma_{ik}(\boldsymbol{q}_i), & \text{for } \varsigma_{ik}(\boldsymbol{q}_i) > 0 \\ [0, 1] \nabla \varsigma_{ik}(\boldsymbol{q}_i), & \text{for } \varsigma_{ik}(\boldsymbol{q}_i) = 0 \\ \boldsymbol{0}_2, & \text{for } \varsigma_{ik}(\boldsymbol{q}_i) < 0 \end{cases}$$

with [0, 1] is a set-valued map with image in the scope [0, 1].

Remark 2: For the quadratic optimization in (27), the number of safety constraints $\mathcal{U}_{ij}$ and $\mathcal{U}_{io}$ increases proportionally with the number of vehicles and obstacles involved, which may result that the collision avoidance becomes much more complicated. But the model complexity of the proposed RNN (28) only depends on the control inputs without considering the number of constraints. Therefore, the proposed neurodynamic optimization method is reasonable and feasible.

Remark 3: The predefined performance function [11], artificial potential function [13], model predictive control [16], and self-motion [45] are common collision avoidance techniques, and usually incorporated in the control law. Compared with these strategies, the proposed FTCBF-based method converts safety objectives into guidance constraints, which are independent of the control law. Besides, it is capable of degrading the tracking performance less when the collision avoidance behavior occurs by solving the constrained optimization problem.

C. Finite-Time Control Law

The last section developed a distributed finite-time safety-critical guidance law for under-actuated MSVs. This section design a finite-time control law at the kinetic level.

By using the optimal guidance signal from (28), the desired heading angle ψ_{ig} is calculated as follows:

$$\psi_{ig} = \operatorname{atan2}\left(q_i^{x*}, q_i^{y*}\right) \tag{29}$$

where $\operatorname{atan2}(\cdot, \cdot)$ is an arctangent function defined as the angle in the Euclidean plane expect $(0, 0)$.

Define a heading tracking error $\psi_{ie} = \psi_i - \psi_{ig}$ and take its time derivative as follows:

$$\dot{\psi}_{ie} = r_i - \dot{\psi}_{ig}. \tag{30}$$

To stabilize $\dot{\psi}_{ie}$, a finite-time virtual control law is developed as follows:

$$r_{ig} = -\mu_{ig}^r \lceil \psi_{ie} \rfloor^{\frac{1}{2}} + \dot{\psi}_{ig} \tag{31}$$

where $\mu_{ig}^r \in \mathbb{R}^+$ is a constant.

Substituting (31) into (30), $\dot{\psi}_{ie}$ is presented as follows:

$$\dot{\psi}_{ie} = -\mu_{ig}^r \lceil \psi_{ie} \rfloor^{\frac{1}{2}} - \tilde{r}_i + \hat{r}_{ie} \tag{32}$$

where $\hat{r}_{ie} = \hat{r}_i - r_{ig}$.

Then, the optimal yaw rate r_i^* under the constraint (7a) is solved by the following quadratic optimization:

$$\begin{aligned} r_i^* = \underset{r_i \in \mathbb{R}}{\operatorname{argmin}} \ & J_i^r(r_i) = \left(r_i - r_{ig}\right)^2 \\ \text{s.t.} \ & r_{i\min} \le r_i \le r_{i\max} \end{aligned} \tag{33}$$

where $r_i^* = \max\{\min\{r_{ig}, r_{i\max}\}, r_{i\min}\}$.

Define the velocity tracking error $\hat{\boldsymbol{\vartheta}}_{ie} = [\hat{\boldsymbol{q}}_{ie}^{\mathrm{T}}, \hat{r}_{ie}]^{\mathrm{T}}$ with $\hat{\boldsymbol{q}}_{ie} = \hat{\boldsymbol{q}}_i - \boldsymbol{q}_i^*$ and $\hat{r}_{ie} = \hat{r}_i - r_i^*$. Then, it gets the derivatives of $\hat{\boldsymbol{\vartheta}}_{ie}$ along (15) as

$$\dot{\hat{\boldsymbol{\vartheta}}}_{ie} = -\mu_{i2} L_i^{\frac{2}{3}} \left\lceil \tilde{\boldsymbol{\eta}}_i \right\rfloor^{\frac{1}{3}} + \hat{\boldsymbol{\zeta}}_{ib} + \boldsymbol{\tau}_{ic} + \boldsymbol{\tau}_{ie} - \dot{\boldsymbol{\vartheta}}_i^* \tag{34}$$

where $\boldsymbol{\tau}_{ie} = \boldsymbol{\tau}_{ib} - \boldsymbol{\tau}_{ic}$ and $\dot{\boldsymbol{\vartheta}}_i^* = [\dot{\boldsymbol{q}}_i^{*T}, \dot{r}_i^*]^{\mathrm{T}}$ with $\boldsymbol{\tau}_{ic} \in \mathbb{R}^3$ being a nominal kinetic control input.

To stabilize the error dynamics in (34), a nominal finite-time kinetic control law is developed by using the estimated disturbance from the RED-based FTSO

$$\boldsymbol{\tau}_{ic} = -\boldsymbol{\mu}_{ic} \left\lceil \hat{\boldsymbol{\vartheta}}_{ie} \right\rfloor^{\frac{1}{2}} - \hat{\boldsymbol{\zeta}}_{ib} - \left[d_i \boldsymbol{p}_{ie}^{\mathrm{T}}, \psi_{ie}\right]^{\mathrm{T}} \tag{35}$$

where $\boldsymbol{\mu}_{ic} = \operatorname{diag}\{\mu_{ic}^q, \mu_{ic}^q, \mu_{ic}^r\}$ with $\mu_{ic}^q \in \mathbb{R}^+$ and $\mu_{ic}^r \in \mathbb{R}^+$.

To acquire the optimal control inputs under input constraints (7b), a quadratic optimization is applied as follows:

$$\begin{aligned} \boldsymbol{\tau}_{ib}^* = \underset{\boldsymbol{\tau}_{ib} \in \mathbb{R}^3}{\operatorname{argmin}} \ & J_i^{\tau}(\boldsymbol{\tau}_{ib}) = \|\boldsymbol{\tau}_{ib} - \boldsymbol{\tau}_{ic}\|^2 \\ \text{s.t.} \ & m_i^u \|\boldsymbol{\tau}_{ib}^q\| \le \tau_{i\max}^u \\ & \tau_{i\min}^r \le m_i^r \tau_{ib}^r \le \tau_{i\max}^r \end{aligned} \tag{36}$$

with $\boldsymbol{\tau}_{ib}^* = [(\boldsymbol{\tau}_{ib}^{q*})^{\mathrm{T}}, \tau_{ic}^{r*}]^{\mathrm{T}}$ and $\boldsymbol{\tau}_{ic} = [(\boldsymbol{\tau}_{ic}^q)^{\mathrm{T}}, \tau_{ic}^r]^{\mathrm{T}}$. As a result, the optimal surge force and yaw moment are deduced as follows:

$$\begin{cases} \tau_i^u = m_i^u \left(\tau_{ib}^{x*} \cos\psi_i + \tau_{ib}^{y*} \sin\psi_i\right) \\ \tau_i^r = m_i^r \tau_{ib}^{r*}. \end{cases} \tag{37}$$

Substituting (35) into (34), one has

$$\dot{\hat{\boldsymbol{\vartheta}}}_{ie} = -\boldsymbol{\mu}_{ic}\left\lceil \hat{\boldsymbol{\vartheta}}_{ie} \right\rfloor^{\frac{1}{2}} - \mu_{i2}L_i^{\frac{2}{3}}\left\lceil \tilde{\boldsymbol{\eta}}_i \right\rfloor^{\frac{1}{3}} - \dot{\boldsymbol{\vartheta}}_i^* + \boldsymbol{\tau}_{ie}^q - \left[d_i\boldsymbol{p}_{ie}^{\mathrm{T}}, \psi_{ie}\right]^{\mathrm{T}}. \tag{38}$$

IV. Stability and Safety Analysis

In the last section, the output-feedback finite-time safety-critical coordinated control method is proposed. In this section, the stability of the closed-loop system is analyzed, and the safety of the multi-MSV system is proved.

A. Finite-Time Safety Analysis

At first, the following lemma gives the finite-time convergence of the neurodynamic optimization (28).

Lemma 2 [44]: For a sufficiently small ι_i, the neuronal state $\boldsymbol{q}_i$ in the RNN (28) can rapidly converge to the optimal guidance signal $\boldsymbol{q}_i^*$ within finite time and hold there in future.

The following lemma shows that the multi-MSV system is safe by using the optimal safety-critical guidance signal $\boldsymbol{q}_i^*$.

Lemma 3: For under-actuated MSVs with dynamics (7), the formation safety of the multi-MSV system is able to be ensured if the velocity signal $\boldsymbol{q}_i$ of underactuated MSVs satisfies all collision-free constraints $\mathcal{U}_{ij}(\boldsymbol{q}_i), j \in \mathcal{V}^F\backslash\{i\}$ and $\mathcal{U}_{io}(\boldsymbol{q}_i), o = 1, \ldots, N_o$.

Proof: According to Lemma 2, the velocity signal $\boldsymbol{q}_i$ can converge to the optimal safety-critical guidance velocity $\boldsymbol{q}_i^*$ within finite time while satisfying all collision-free constraints. From Lemma 1, the optimal signal $\boldsymbol{q}_i^*$ is able to guarantee that the sets $\mathcal{C}_{ij}$ and $\mathcal{C}_{io}$ are forward invariant for the initial state $\boldsymbol{p}_i(t_0) \in \mathcal{C}_{ij} \cap \mathcal{C}_{io}$, i.e., $\mathcal{C}_{ij}$ and $\mathcal{C}_{io}$ are safe sets. If $\boldsymbol{p}_i(t_0) \notin \mathcal{C}_{ij} \cup \mathcal{C}_{io}$, the optimal guidance signal $\boldsymbol{q}_i^*$ drives the MSV to the safe zone within a finite time t_1, i.e., $\boldsymbol{p}_i(t) \in \mathcal{C}_{ij} \cap \mathcal{C}_{io}$ for $t > t_1$. It implies that $\mathcal{C}_{ij}$ and $\mathcal{C}_{io}$ are forward invariant for $\boldsymbol{p}_i(t) \in \mathcal{C}_{ij} \cap \mathcal{C}_{io}$, $t > t_1$. Thus, the optimal safety-critical guidance signals can ensure the safety of the multi-MSV system. ■

B. Closed-Loop Subsystem Analysis

Recall the error dynamics as follows:

$$\begin{cases} \dot{\boldsymbol{p}}_{ie} = -\mu_{ig}^q\left\lceil \boldsymbol{p}_{ie} \right\rfloor^{\frac{1}{2}} + d_i\hat{\boldsymbol{q}}_{ie} + \sum_{j\in\mathcal{N}_i^F} a_{ij}\tilde{\boldsymbol{q}}_j \\ \qquad - d_i\tilde{\boldsymbol{q}}_i - \sum_{k\in\mathcal{N}_i^L} a_{ik}\boldsymbol{p}_{kr}^{\theta}\chi_k \\ \dot{\psi}_{ie} = -\mu_{ig}^r\left\lceil \psi_{ie} \right\rfloor^{\frac{1}{2}} - \tilde{r}_i + \hat{r}_{ie} \\ \dot{\hat{\boldsymbol{\vartheta}}}_{ie} = -\boldsymbol{\mu}_{ic}\left\lceil \hat{\boldsymbol{\vartheta}}_{ie} \right\rfloor^{\frac{1}{2}} - \mu_{i2}L_i^{\frac{2}{3}}\left\lceil \tilde{\boldsymbol{\eta}}_i \right\rfloor^{\frac{1}{3}} - \dot{\boldsymbol{\vartheta}}_i^* \\ \qquad + \boldsymbol{\tau}_{ie}^q - \left[d_i\boldsymbol{p}_{ie}^{\mathrm{T}}, \psi_{ie}\right]^{\mathrm{T}} \\ \dot{\bar{\theta}}_{ke} = -\chi_k. \end{cases} \tag{39}$$

The following lemma shows the stability of the total closed-loop system (39).

Lemma 4: Under Assumptions 1 and 2, the error signals of the total closed-loop system (39) are uniformly ultimately bounded.

Proof: Consider a Lyapunov function candidate as follows:

$$V_2 = \frac{1}{2}\sum_{i=1}^{M}\left(\boldsymbol{p}_{ie}^{\mathrm{T}}\boldsymbol{p}_{ie} + \hat{\boldsymbol{q}}_{ie}^{\mathrm{T}}\hat{\boldsymbol{q}}_{ie} + \psi_{ie}^2 + \hat{r}_{ie}^2\right) + \frac{1}{2}\bar{\boldsymbol{\theta}}_e^{\mathrm{T}}\mathcal{H}\bar{\boldsymbol{\theta}}_e.$$

Taking the time derivative of V_2 with (39), it yields that

$$\begin{aligned} \dot{V}_2 = \sum_{i=1}^{M}\Bigg\{ & -\mu_{ig}^q\boldsymbol{p}_{ie}^{\mathrm{T}}\left\lceil \boldsymbol{p}_{ie} \right\rfloor^{\frac{1}{2}} - \sum_{k\in\mathcal{N}_i^L} a_{ik}\boldsymbol{p}_{ie}^{\mathrm{T}}\boldsymbol{p}_{kr}^{\theta}\chi_k \\ & - d_i\boldsymbol{p}_{ie}^{\mathrm{T}}\tilde{\boldsymbol{q}}_i + \sum_{j\in\mathcal{N}_i^F} a_{ij}\boldsymbol{p}_{ie}^{\mathrm{T}}\tilde{\boldsymbol{q}}_j - \mu_{ic}^q\hat{\boldsymbol{q}}_{ie}^{\mathrm{T}}\left\lceil \hat{\boldsymbol{q}}_{ie} \right\rfloor^{\frac{1}{2}} \\ & - \mu_{i2}L_i^{\frac{2}{3}}\hat{\boldsymbol{q}}_{ie}^{\mathrm{T}}\left\lceil \tilde{\boldsymbol{p}}_i \right\rfloor^{\frac{1}{3}} - \hat{\boldsymbol{q}}_{ie}^{\mathrm{T}}\left(\dot{\boldsymbol{q}}_i^* - \boldsymbol{\tau}_{ie}^q\right) - \psi_{ie}\tilde{r}_i \\ & - \mu_{ig}^r|\psi_{ie}|^{\frac{3}{2}} - \mu_{ic}^r|\hat{r}_{ie}|^{\frac{3}{2}} - \mu_{i2}^r L_i^{\frac{2}{3}}\hat{r}_{ie}\left\lceil \tilde{\psi}_i \right\rfloor^{\frac{1}{3}} \\ & - \hat{r}_{ie}\dot{r}_i^* + \hat{r}_{ie}\tau_{ie}^r\Bigg\} - \sum_{k=M+1}^{N}\chi_k\theta_{ke}. \end{aligned} \tag{40}$$

Substituting (20) into (40), one has

$$\begin{aligned} \dot{V}_2 = & \sum_{i=1}^{M}\Bigg\{ - \mu_{ig}^q\boldsymbol{p}_{ie}^{\mathrm{T}}\left\lceil \boldsymbol{p}_{ie} \right\rfloor^{\frac{1}{2}} - d_i\boldsymbol{p}_{ie}^{\mathrm{T}}\tilde{\boldsymbol{q}}_i - \mu_{ic}^q\hat{\boldsymbol{q}}_{ie}^{\mathrm{T}}\left\lceil \hat{\boldsymbol{q}}_{ie} \right\rfloor^{\frac{1}{2}} \\ & + \sum_{j\in\mathcal{N}_i^F} a_{ij}\boldsymbol{p}_{ie}^{\mathrm{T}}\tilde{\boldsymbol{q}}_j - \mu_{i2}L_i^{\frac{2}{3}}\hat{\boldsymbol{q}}_{ie}^{\mathrm{T}}\left\lceil \tilde{\boldsymbol{p}}_i \right\rfloor^{\frac{1}{3}} - \mu_{ig}^r|\psi_{ie}|^{\frac{3}{2}} \\ & - \hat{\boldsymbol{q}}_{ie}^{\mathrm{T}}\left(\dot{\boldsymbol{q}}_i^* - \boldsymbol{\tau}_{ie}^q\right) - \mu_{ic}^r|\hat{r}_{ie}|^{\frac{3}{2}} - \mu_{i2}L_i^{\frac{2}{3}}\hat{r}_{ie}\left\lceil \tilde{\psi}_i \right\rfloor^{\frac{1}{3}} \\ & - \psi_{ie}\tilde{r}_i - \hat{r}_{ie}\left(\dot{r}_i^* - \tau_{ie}^r\right)\Bigg\} - \sum_{k=M+1}^{N}\mu_{kg}^{\chi}e_k^{\frac{3}{2}} \\ \le & \sum_{i=1}^{M}\Bigg\{ - \mu_{ig}^q\|\boldsymbol{p}_{ie}\|^{\frac{3}{2}} - \mu_{ic}^q\|\hat{\boldsymbol{q}}_{ie}\|^{\frac{3}{2}} - \mu_{ig}^r|\psi_{ie}|^{\frac{3}{2}} \\ & - \mu_{ic}^r|\hat{r}_{ie}|^{\frac{3}{2}} + \|\boldsymbol{p}_{ie}\|\|\sum_{j\in\mathcal{N}_i^F} a_{ij}\tilde{\boldsymbol{q}}_j - d_i\tilde{\boldsymbol{q}}_i\| \\ & + \|\hat{\boldsymbol{q}}_{ie}\|\|\mu_{i2}L_i^{\frac{2}{3}}\left\lceil \tilde{\boldsymbol{p}}_i \right\rfloor^{\frac{1}{3}} + \dot{\boldsymbol{q}}_i^* - \boldsymbol{\tau}_{ie}^q\| + |\psi_{ie}||\tilde{r}_i| \\ & + |\hat{r}_{ie}||\mu_{i2}L_i^{\frac{2}{3}}\left\lceil \tilde{\psi}_i \right\rfloor^{\frac{1}{3}} + \dot{r}_i^* - \tau_{ie}^r|\Bigg\} - \sum_{k=M+1}^{N}\mu_{kg}^{\chi}e_k^{\frac{3}{2}}. \end{aligned} \tag{41}$$

Letting $\underline{\mu}_i = \min_{i=1,\ldots,M}\{\mu_{ig}^q, \mu_{ic}^q, \mu_{ig}^r, \mu_{ic}^r\}$, we rewrite $\dot{V}_2$ as follows:

$$\begin{aligned} \dot{V}_2 \le & \sum_{i=1}^{M}\Bigg\{ -\underline{\mu}_i\left(\|\boldsymbol{p}_{ie}\|^{\frac{3}{2}} + \|\hat{\boldsymbol{q}}_{ie}\|^{\frac{3}{2}} + |\psi_{ie}|^{\frac{3}{2}} + |\hat{r}_{ie}|^{\frac{3}{2}}\right) \\ & + |\sigma_i|\|\boldsymbol{p}_{ie}\|\|\tilde{\boldsymbol{q}}_i\| + \|\hat{\boldsymbol{q}}_{ie}\|\|\mu_{i2}L_i^{\frac{2}{3}}\left\lceil \tilde{\boldsymbol{p}}_i \right\rfloor^{\frac{1}{3}} + \dot{\boldsymbol{q}}_i^* - \boldsymbol{\tau}_{ie}^q\| \\ & + |\psi_{ie}||\tilde{r}_i| + |\hat{r}_{ie}||\mu_{i2}L_i^{\frac{2}{3}}\left\lceil \tilde{\psi}_i \right\rfloor^{\frac{1}{3}} + \dot{r}_i^* - \tau_{ie}^r|\Bigg\} \\ & - \sum_{k=M+1}^{N}\mu_{kg}^{\chi}e_k^{\frac{3}{2}} \end{aligned} \tag{42}$$

with $\sigma_i = \sum_{j\in\mathcal{N}_i^F} a_{ij} - d_i$.

By Lemma 2, the derivatives of $\dot{\boldsymbol{q}}_i^*$ and $\dot{r}_i^*$ are bounded and satisfied with $\|\dot{\boldsymbol{q}}_i^*\| \le \bar{q}_i^* \in \mathbb{R}^+$ and $|\dot{r}_i^*| \le \bar{r}_i^* \in \mathbb{R}^+$. Limited by the actuator power of a practical MSV, it is obvious that the control input errors $\boldsymbol{\tau}_{ie}^q$ and τ_{ie}^r satisfy $\|\boldsymbol{\tau}_{ie}^q\| \le \bar{\tau}_{ie}^q \in \mathbb{R}^+$

and $|\tau_{ie}^r| \le \bar{\tau}_{ie}^r \in \mathbb{R}^+$. Using $\|\tilde{\boldsymbol{p}}_i\| \le \bar{\eta}_i$, $\|\tilde{\psi}_i\| \le \bar{\eta}_i$, $\|\tilde{\boldsymbol{q}}_i\| \le \bar{\vartheta}_i$ and $\|\tilde{r}_i\| \le \bar{\vartheta}_i$, $\dot{V}_2$ is further deduced as follows:

$$\begin{aligned}\dot{V}_2 \le \sum_{i=1}^{M}\Big\{&-\underline{\mu}_i\Big(\|\boldsymbol{p}_{ie}\|^{\frac{3}{2}} + \|\hat{\boldsymbol{q}}_{ie}\|^{\frac{3}{2}} + |\psi_{ie}|^{\frac{3}{2}} + |\hat{r}_{ie}|^{\frac{3}{2}}\Big)\\ &+ \bar{\vartheta}_i|\sigma_i|\|\boldsymbol{p}_{ie}\| + \|\hat{\boldsymbol{q}}_{ie}\|\Big(\mu_{i2}L_i^{\frac{2}{3}}\bar{\eta}_i^{\frac{1}{3}} + \bar{q}_i^* + \bar{\tau}_{ie}^q\Big)\\ &+ \bar{\vartheta}_i|\psi_{ie}| + |\hat{r}_{ie}|\Big(\mu_{i2}L_i^{\frac{2}{3}}\bar{\eta}_i^{\frac{1}{3}} + \bar{r}_i^* + \bar{\tau}_{ie}^r\Big)\Big\}\\ &- \sum_{k=M+1}^{N}\mu_{kg}^{\chi}e_k^{\frac{3}{2}}.\end{aligned} \tag{43}$$

Rewrite (43) as follows:

$$\begin{aligned}\dot{V}_2 \le \sum_{i=1}^{M}\Big\{&-\underline{\mu}_i\Big(\|\boldsymbol{p}_{ie}\|^{\frac{3}{2}} + \|\hat{\boldsymbol{q}}_{ie}\|^{\frac{3}{2}} + |\psi_{ie}|^{\frac{3}{2}} + |\hat{r}_{ie}|^{\frac{3}{2}}\Big)\\ &+ \xi_i\big(\|\boldsymbol{p}_{ie}\| + \|\hat{\boldsymbol{q}}_{ie}\| + |\psi_{ie}| + |\hat{r}_{ie}|\big)\Big\} - \sum_{k=M+1}^{N}\mu_{kg}^{\chi}e_k^{\frac{3}{2}}.\end{aligned} \tag{44}$$

where $\xi_i = \max\{\xi_{i1}, \xi_{i2}, \xi_{i3}, \xi_{i4}\}$ with $\xi_{i1} = \bar{\vartheta}_i|\sigma_i|$, $\xi_{i2} = \mu_{i2}L_i^{\frac{2}{3}}\bar{\eta}_i^{\frac{1}{3}} + \bar{q}_i^* + \bar{\tau}_{ie}^q$, $\xi_{i3} = \bar{\vartheta}_i$ and $\xi_{i4} = \mu_{i2}L_i^{\frac{2}{3}}\bar{\eta}_i^{\frac{1}{3}} + \bar{r}_i^* + \bar{\tau}_{ie}^r$.

Define the vector $\boldsymbol{E}' = [\boldsymbol{p}_e^{\mathrm{T}}, \hat{\boldsymbol{q}}_e^{\mathrm{T}}, \boldsymbol{\psi}_e^{\mathrm{T}}, \hat{\boldsymbol{r}}_e^{\mathrm{T}}, \boldsymbol{e}^{\mathrm{T}}]^{\mathrm{T}}$ with $\boldsymbol{p}_e = [\boldsymbol{p}_{1e}^{\mathrm{T}}, \ldots, \boldsymbol{p}_{Me}^{\mathrm{T}}]^{\mathrm{T}}$, $\hat{\boldsymbol{q}}_e = [\hat{\boldsymbol{q}}_{1e}^{\mathrm{T}}, \ldots, \hat{\boldsymbol{q}}_{Me}^{\mathrm{T}}]^{\mathrm{T}}$, $\boldsymbol{\psi}_e = [\psi_{1e}, \ldots, \psi_{Me}]^{\mathrm{T}}$ $\hat{\boldsymbol{r}}_e = [r_{1e}, \ldots, r_{Me}]^{\mathrm{T}}$, $\boldsymbol{e} = [e_{M+1}, \ldots, e_N]^{\mathrm{T}}$ and $\boldsymbol{E} = [\boldsymbol{p}_e^{\mathrm{T}}, \hat{\boldsymbol{q}}_e^{\mathrm{T}}, \boldsymbol{\psi}_e^{\mathrm{T}}, \hat{\boldsymbol{r}}_e^{\mathrm{T}}, \bar{\boldsymbol{\theta}}_e^{\mathrm{T}}]^{\mathrm{T}}$. Then, one has $\dot{V}_2 \le -c_1\|\boldsymbol{E}\|^{(3/2)} + |\Xi|\|\boldsymbol{E}\|$, where $c_1 = \min_{i=1,\ldots,M,k=M+1,\ldots,N}\{-\underline{\mu}_i, \mu_{kg}^{\chi}\}$ and $\Xi = \max_{i=1,\ldots,M}\{\xi_i\}$.

Applying the change $\boldsymbol{E}' = \boldsymbol{\Psi}\boldsymbol{E}$ with

$$\boldsymbol{\Psi} = \begin{bmatrix} \boldsymbol{I}_N \otimes \boldsymbol{I}_2 & \boldsymbol{0} & \boldsymbol{0} & \boldsymbol{0} & \boldsymbol{0} \\ \boldsymbol{0} & \boldsymbol{I}_N \otimes \boldsymbol{I}_2 & \boldsymbol{0} & \boldsymbol{0} & \boldsymbol{0} \\ \boldsymbol{0} & \boldsymbol{0} & \boldsymbol{I}_N & \boldsymbol{0} & \boldsymbol{0} \\ \boldsymbol{0} & \boldsymbol{0} & \boldsymbol{0} & \boldsymbol{I}_N & \boldsymbol{0} \\ \boldsymbol{\Phi} & \boldsymbol{0} & \boldsymbol{0} & \boldsymbol{0} & -\mathcal{H} \end{bmatrix}$$

$$\boldsymbol{\Phi} = \begin{bmatrix} a_{(M+1)1}\frac{\partial p_{(M+1)r}}{\partial \theta_{M+1}} & \cdots & a_{(M+1)M}\frac{\partial p_{(M+1)r}}{\partial \theta_{N+M}} \\ \vdots & \ddots & \vdots \\ a_{NN}\frac{\partial p_{Nr}}{\partial \theta_N} & \cdots & a_{NM}\frac{\partial p_{Nr}}{\partial \theta_N} \end{bmatrix}$$

and $\|\boldsymbol{E}'\| \ge \lambda_{\min}(\boldsymbol{\Psi})\|\boldsymbol{E}\|$, it renders that

$$\dot{V}_2 \le -c_1\lambda_{\min}^{\frac{3}{2}}(\boldsymbol{\Psi})\|\boldsymbol{E}\|^{\frac{3}{2}} + |\Xi|\|\boldsymbol{E}\| \tag{45}$$

where $\lambda_{\min}(\boldsymbol{\Psi})$ is the minimum singular value of $\boldsymbol{\Psi}$.

For $\|\boldsymbol{E}\|^{(1/2)} \ge |\Xi|/(c_1\lambda_{\min}^{(3/2)}(\boldsymbol{\Psi}))$, we have $\dot{V}_2 \le -c_2V_2^{(3/4)}$, where $c_2 = (c_1\lambda_{\min}^{(3/2)}(\boldsymbol{\Psi}) - |\Xi|/\|\boldsymbol{E}\|^{(1/2)})(2/c_3)^{(3/4)}$ with $c_3 = \max\{1, \lambda_{\max}(\mathcal{H})\}$. According to [46, Lemma 1], $\boldsymbol{E}$ converges to the region $\|\boldsymbol{E}\|^{(1/2)} \le |\Xi|/(c_1\lambda_{\min}^{(3/2)}(\boldsymbol{\Psi}))$ within a finite time T, satisfying $T \le 4V_2^{(1/4)}/c_2$. In conclusion, the tracking error $\boldsymbol{E}$ of the total closed-loop system converges to $\|\boldsymbol{E}\| \le |\Xi|^2/(c_1^2\lambda_{\min}^3(\boldsymbol{\Psi}))$ in T. ■

Remark 4: It is seen that the error $\|\boldsymbol{E}\|$ will increase as the number of individuals in the multi-MSV formation. And the upper bound of the error $\|\boldsymbol{E}\|$ is reflected by the communication topology. But the information of all vehicles is not needed in the controller design. Thus, the proposed method is still distributed.

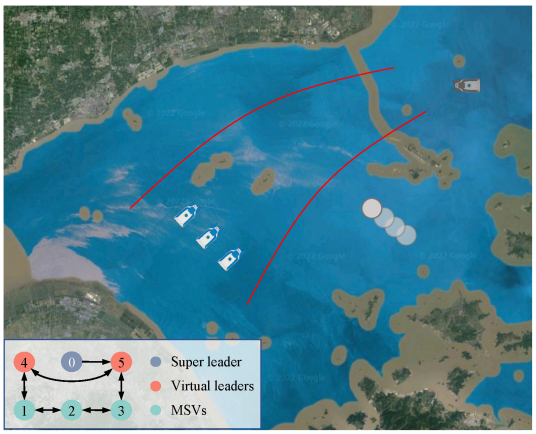

Fig. 4. Application case of multi-MSV formation on an unsafe water.

C. Stability and Safety Analysis

This section analyzes the stability of the closed-loop system and the safety of the multi-MSV system and provides the following theorem.

Theorem 1: Consider a formation of multiple under-actuated MSVs with model (5), velocity constraints (7a), and input constraints (7b). Under Assumptions 1 and 2, the multi-MSV system is safety-critical by using the RED-based FTSO (15), the distributed finite-time safety-critical guidance law (28), and the finite-time control law (36), i.e., there is no collision among neighboring MSVs and between MSVs and static/moving obstacles. And error signals of the total closed-loop system are uniformly ultimately bounded.

Proof: Letting $\boldsymbol{p} = [\boldsymbol{p}_1^{\mathrm{T}}, \ldots, \boldsymbol{p}_M^{\mathrm{T}}]^{\mathrm{T}}$ and $\boldsymbol{p}_r = [\boldsymbol{p}_{(M+1)r}^{\mathrm{T}}, \ldots, \boldsymbol{p}_{Nr}^{\mathrm{T}}]^{\mathrm{T}}$, one has $\boldsymbol{p}_e = (\boldsymbol{L}_1 \otimes \boldsymbol{I}_2)\boldsymbol{p} + (\boldsymbol{L}_2 \otimes \boldsymbol{I}_2)\boldsymbol{p}_r = (\boldsymbol{L}_1 \otimes \boldsymbol{I}_2)(\boldsymbol{p} + (\boldsymbol{L}_1^{-1}\boldsymbol{L}_2 \otimes \boldsymbol{I}_2)\boldsymbol{p}_r)$. Further, it devises that $\|\boldsymbol{p} + (\boldsymbol{L}_1^{-1}\boldsymbol{L}_2 \otimes \boldsymbol{I}_2)\boldsymbol{p}_r\| \le \|\boldsymbol{p}_e\|/\lambda_{\min}(\boldsymbol{L}_1)$. From Assumption 1 and Lemma 4, the errors $\boldsymbol{p}_e$ and $\bar{\boldsymbol{\theta}}_e$ are bounded. It means that there exist positive constant δ_i and δ_{k2} such that the geometric objective (10) and the dynamic objective (12), respectively. Then, it gets that the error χ_k is bounded. Thus, it infers that there exists a positive constant δ_{k1} and the dynamic objective (11) is achieved. By Lemmas 2 and 3, it is proved that the constraints (27), (33), and (36), are satisfied by using the optimal signals $\boldsymbol{\vartheta}_i^*$ and $\boldsymbol{\tau}_{ib}^*$. It shows that the closed-loop multi-MSV system is safety-critical without violating the velocity and input constraints, i.e., safety objectives (13) and (14) are achieved. ■

V. Simulation Results

This section gives simulation results for an application case to demonstrate the effectiveness of the proposed output-feedback finite-time safety-critical coordinated control method. As shown in Fig. 4, three under-actuated MSVs, labeled as 1∼3, perform tasks guided by two virtual leaders, labeled as 4, 5, and one super leader labeled as 0, and sail on waters with multiple static/moving obstacles, such as

TABLE I
INITIAL STATUS OF THE MSVS AND STATIC/MOVING OBSTACLES

$i=1,2,3,o$	MSV1	MSV2	MSV3	MSVo
$[\boldsymbol{p}_i^T,\ \psi_i]$	[35, -15, π]	[40, 0, π]	[40, -10, π]	[120, 80, π]
$[\boldsymbol{q}_i^T, r_i]$	[0, 0, 0]	[0, 0, 0]	[0, 0, 0]	[-0.12, 0, 0]
$o=1,2,3,4$	Obstacle1	Obstacle2	Obstacle3	Obstacle4
$\boldsymbol{p}_o^T$	[-10, 30]	[25, 80]	[75, 60]	[35, 35]
$\boldsymbol{q}_o^T$	[0, 0]	[0, 0]	[0, 0]	[0, 0.2]
ρ_o	4	3	5	3

TABLE II
ALL PARAMETERS OF THE DPM-FTCBF METHOD

Symbol	L_i	μ_{i1}	μ_{i2}	μ_{i3}	μ_{kg}^{χ}	μ_{ig}^{q}	μ_{ig}^{r}
Value	3.5	4	5.6	1.1	2	0.2	0.6
Symbol	μ_{ic}^{q}	μ_{ic}^{r}	$\varkappa_{ij}$	$\varkappa_{io}$	β_{ij}	β_{io}	ϵ_i
Value	0.6	1.2	2	2	0.5	0.5	1
Symbol	ι_i	D_s	D_o	υ_s	$u_{i\max}$	$v_{i\max}$	$r_{i\max}$
Value	0.5	4	2	0.5	0.8	0.2	0.5
Symbol	$u_{i\min}$	$v_{i\min}$	$r_{i\min}$	$\tau_{i\max}^{u}$	$\tau_{i\max}^{r}$		
Value	0	-0.2	-0.5	20	5		

reefs, isolated islands, and sailing ships. Then, one obstructive MSV named as o, three static and one dynamic obstacles named as 1∼4 are set in this simulation. In addition, Fig. 4 also describes the communication topology between MSVs and leaders.

According to [47], we select the vehicle model as $\boldsymbol{M}_i = \text{diag}\{25.8, 33.8, 2.76\}$, $\boldsymbol{D}_i = \text{diag}\{0.7225 + 1.3274|u_i| + 5.8664u_i^2, 0.88965 + 36.47287|v_i| + 0.805|r_i|, 1.90 - 0.08|v_i| + 0.75|r_i|\}$

$$\boldsymbol{C}_i = \begin{bmatrix} 0 & 0 & -33.8v_i - 1.0948r_i \\ 0 & 0 & -25.8u_i \\ 33.8v_i + 1.0948r_i & 25.8u_i & 0 \end{bmatrix}.$$

The external disturbance $\boldsymbol{\tau}_{i\omega}$ is generated via the Gauss–Markov process $\dot{\boldsymbol{\tau}}_{iw} + k_i\boldsymbol{\tau}_{iw} = \boldsymbol{w}_i$, where $k_i \in \mathbb{R}^+$ is a constant, and $\boldsymbol{w}_i$ represents the white noises [48]. The two virtual leaders move along the parameterized paths $\boldsymbol{p}_{4r}(\theta_4) = [40 - 45\sqrt{2}\sin(\upsilon_s\theta_4/45 + \pi/8), 40 - 45\sqrt{2}\cos(\upsilon_s\theta_4/45 + \pi/8)]^{\mathrm{T}}$ and $\boldsymbol{p}_{5r}(\theta_5) = [40 - 20\sqrt{2}\sin(\upsilon_s\theta_5/45 + \pi/8), 40 - 20\sqrt{2}\cos(\upsilon_s\theta_5/45 + \pi/8)]^{\mathrm{T}}$ with $\theta_4(0) = \theta_5(0) = 0$ and $\Theta_4 = \Theta_5 = 0$. To be clear, two tables summary all parameters used in this simulation. Concretely, Table I lists the initial status of three MSVs, one obstructive MSV, three static, and one moving obstacle. Table II provides the relative parameters of the proposed distributed path maneuvering method based on FTCBF (DPM-FTCBF). To further illustrate the efficacy and superiority of the DPM-FTCBF method, we employ two comparison methods, i.e., the distributed path maneuvering (DPM) method in [39], and the DPM method based on potential function (DPM-PF) in [15].

Figs. 5–14 shows the simulation results. Specifically, Fig. 5 depicts the geometric pattern of three under-actuated MSVs guided by two virtual leaders based on the DPM-FTCBF

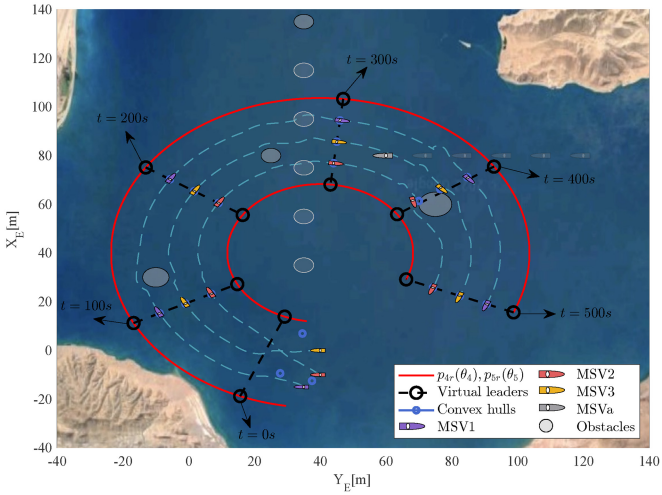

Fig. 5. Formation trajectories of 1–3 MSVs guided by 2 virtual leaders.

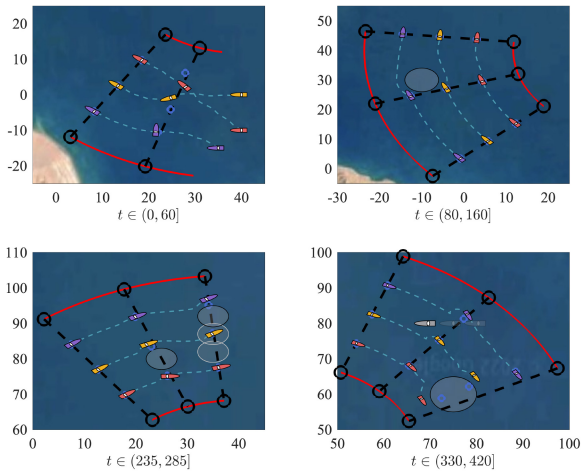

Fig. 6. Four snapshots of multi-MSV formation based on the DPM-FTCBF method.

method. It is seen that these MSVs achieve the desired formation shown in the topology in Fig. 4, while avoiding three static obstacles of different sizes. In order to observer in more detail, Fig. 6 draws the four snapshots of 3 MSVs during 0∼60 s, 80∼160 s, 235∼285 s, and 330∼420 s. For $t \in (0, 60]$, MSV2 and MSV3 move away from each other at the intersection with no collision. For $t \in (80, 160]$, MSV1 and MSV2 bypass the Obstacle1 while maintaining the formation with MSV3. For $t \in (235, 285]$, three MSVs avoid the moving Obstacle4 after dodging the static Obstacle2. For $t \in (330, 420]$, MSV2 and MSV3 move towards their corresponding convex hulls while bypassing Obstacle3. According to four snapshots in Fig. 6, it shows that the safety objectives (13) and (14) are satisfied by using the DPM-FTCBF method. Fig. 7 draws the Euclidean norm of the distributed tracking error $\boldsymbol{p}_{ie}$ in (17) based on the DPM, DPM-FTCBF, and DPM-PF methods, respectively. The errors $\|\boldsymbol{p}_{1e}\|$, $\|\boldsymbol{p}_{2e}\|$, and $\|\boldsymbol{p}_{3e}\|$ based on the DPM method converge to the neighborhood of the origin and do not change afterwards. Due to collision avoidance involved in the DPM-PF and DPM-FTCBF methods, $\|\boldsymbol{p}_{1e}\|$, $\|\boldsymbol{p}_{2e}\|$, and $\|\boldsymbol{p}_{3e}\|$ start to increase when collision avoidance is in effect, and reconverge to the neighborhood

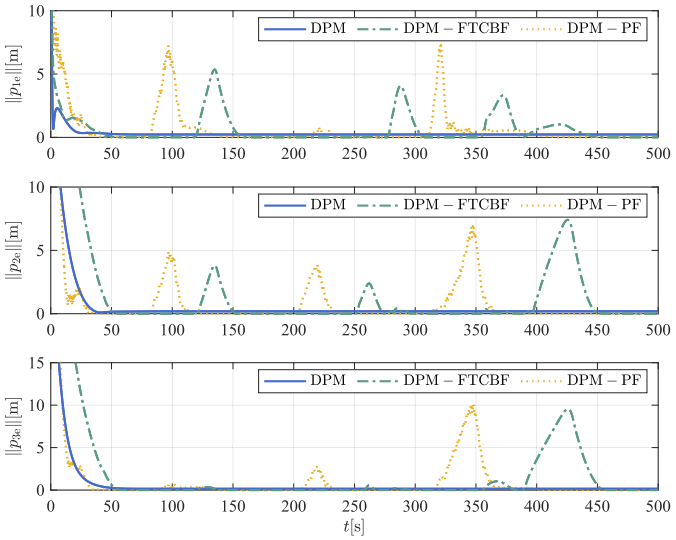

Fig. 7. Earth-fixed distributed tracking errors of MSVs based on the DPM, DPM-FTCBF, and DPM-PF methods.

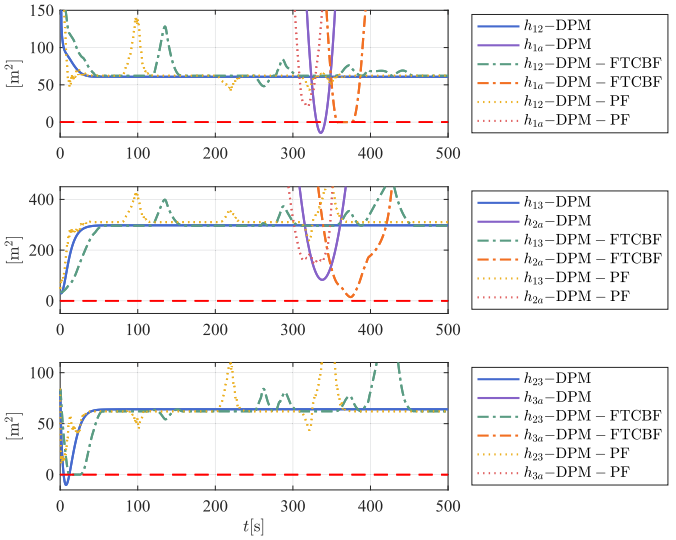

Fig. 8. FTCBFs among MSVs based on the DPM, DPM-FTCBF, and DPM-PF methods.

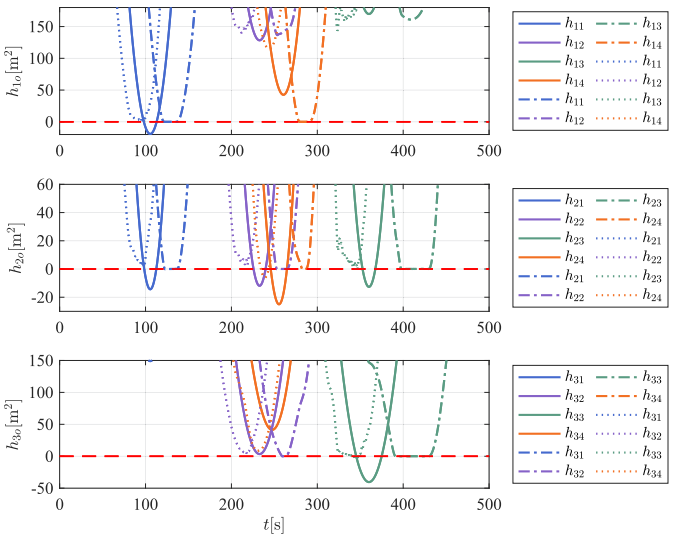

Fig. 9. FTCBFs between MSVs and static/moving obstacles based on the DPM, DPM-FTCBF, and DPM-PF methods.

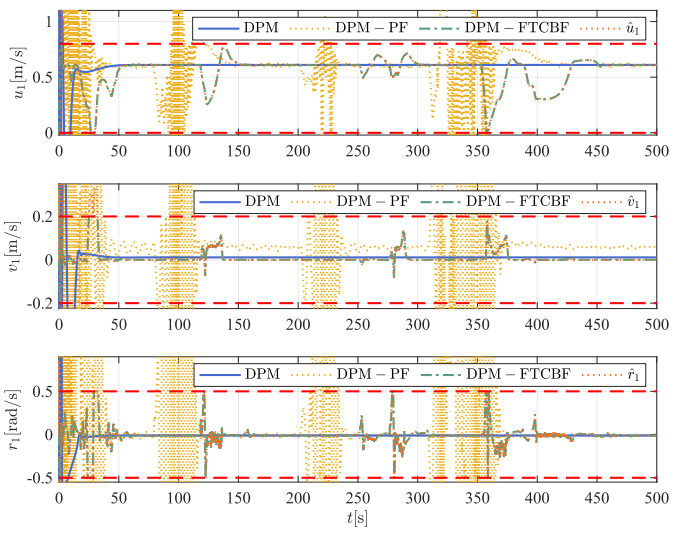

Fig. 10. Earth-fixed velocity signals of MSV1 based on the DPM, DPM-FTCBF, and DPM-PF methods.

of the origin when collision avoidance ends. It can be seen that the DPM-FTCBF-based errors are smaller than that based on the DPM method at steady state. For $t \in (80, 160]$, avoiding the Obstacle1 with the proposed DPM-FTCBF method is capable of less increasing the tracking errors compared with the DPM-PF method, i.e., declining the tracking performance less when collision avoidance. To further explain, Figs. 8 and 9 plot the FTCBFs h_{ij} and h_{io} defined by (24) and (26) based on the three methods. From the definitions of h_{ij} and h_{io}, the non-negative h_{ij} and h_{io} mean the safety objectives (13) and (14) are accomplished. In the third subfigure of Fig. 8, the DPM-based h_{23} from positive to negative means that MSVs 2∼3 collide before converging to convex hulls. In this case, the functions h_{23} with the DPM-PF and DPM-FTCBF methods are always non-negative, which also verifies the first snapshot in Fig. 6. According to the DPM-based h_{1a}, MSV3 will hit the MSVa. Two other methods can ensure the safety of MSV3. According to the dot line h_{24}, the DPM-PF method may fail when both dynamic and static obstacles exist. The DPM-FTCBF method is able to guarantee the critical safety of all MSVs from Figs. 8 and 9. Fig. 10 presents the actual velocities of MSV1 guided by the DPM, DPM-FTCBF, and DPM-PF methods and the estimated values from the FTSO (15). It can be obtained that only the DPM-FTCBF method can force the velocity signals to satisfy the set constraints (7a). Fig. 11 displays the estimated performances for the total disturbances composed of the model uncertainties and environmental disturbances from the FTSO and the ESO. It is found that the FTSO can estimate the disturbance term faster and more accurately. Figs. 12 and 13 draw the surge forces and yaw moments of MSV 1∼3, respectively, where the input constraints (7b) are not violated by using the DPM-FTCBF method. Fig. 13 shows that different bounds affect the convergence speed of tracking errors but not the tracking accuracy in steady state.

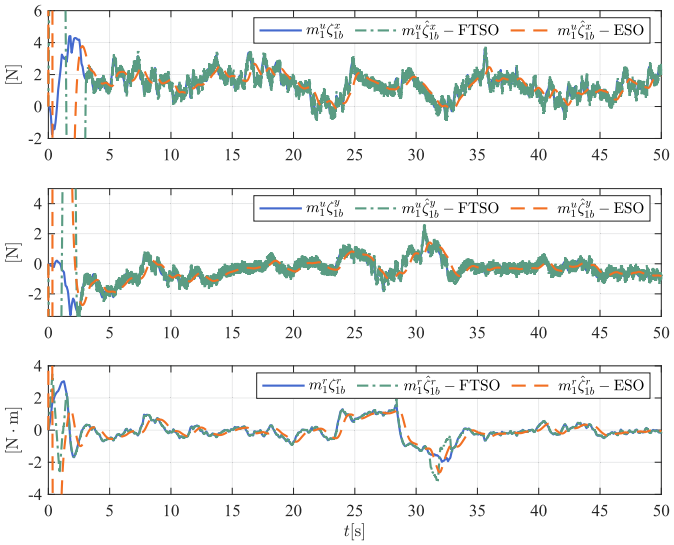

Fig. 11. Earth-fixed total disturbances of MSV1 based on the FTSO and the ESO.

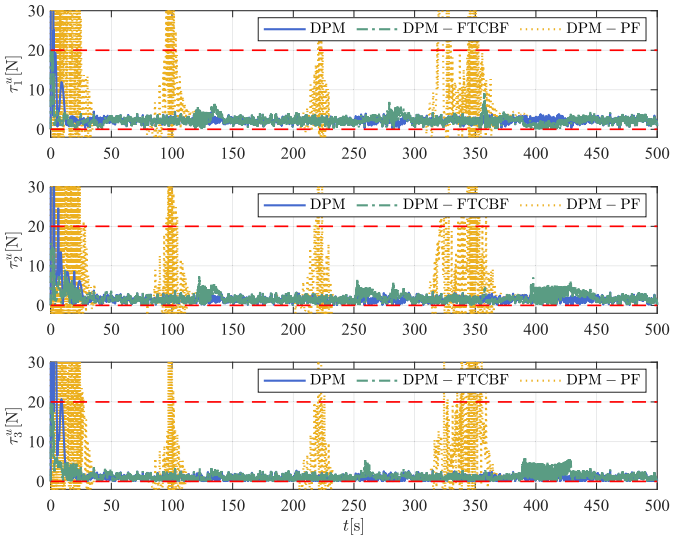

Fig. 12. Surge force of MSVs based on the DPM, DPM-FTCBF, and DPM-PF methods.

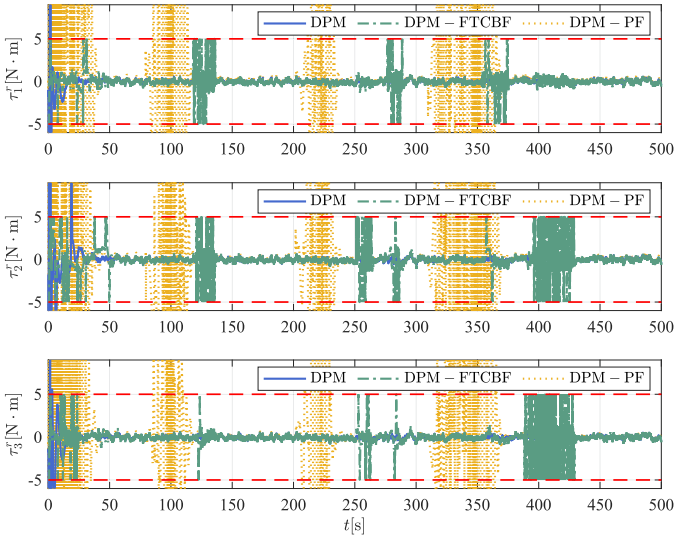

Fig. 13. Yaw moment of MSVs based on the DPM, DPM-FTCBF, and DPM-PF methods.

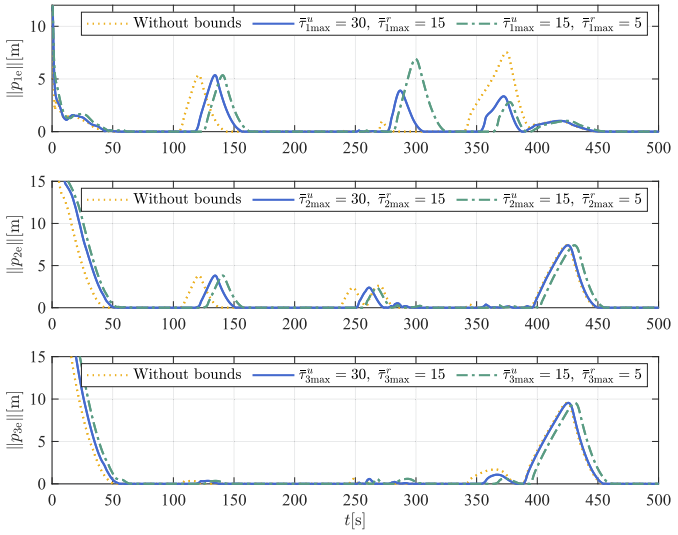

Fig. 14. Earth-fixed distributed tracking errors based on the DPM-FTCBF method under different bounds.

VI. Conclusion

This article proposes an output-feedback finite-time safety-critical coordinated control method for path-guided under-actuated MSVs subject to the static/moving obstacles. Each MSV is also faced with model uncertainties, environmental disturbances, and velocity and input constraints. First, an RED-based FTSO is developed to recovery the unknown velocities and estimate the total disturbances. Next, based on the FTCBFs and neurodynamic optimization technique, a distributed finite-time safety-critical guidance law is designed for under-actuated MSVs by using the estimated information. Then, the tracking errors of the closed-loop system are proved to be uniformly ultimately bounded, and the multi-MSV system is guaranteed to be safety-critical. Simulation results show that the proposed method can achieve the coordinated formation of MSVs and ensure no collisions among neighboring MSVs and between MSVs and static/moving obstacles.

References

[1] N. Gu, D. Wang, Z. Peng, J. Wang, and Q.-L. Han, "Advances in line-of-sight guidance for path following of autonomous marine vehicles: An overview," *IEEE Trans. Syst., Man, Cybern., Syst.*, early access, Apr. 6, 2022, doi: 10.1109/TSMC.2022.3162862.

[2] X. Xiang, C. Yu, L. Lapierre, J. Zhang, and Q. Zhang, "Survey on fuzzy-logic-based guidance and control of marine surface vehicles and underwater vehicles," *Int. J. Fuzzy Syst.*, vol. 20, no. 2, pp. 572–586, Oct. 2018.

[3] X.-M. Zhang *et al.*, "Networked control systems: A survey of trends and techniques," *IEEE/CAA J. Autom. Sinica*, vol. 7, no. 1, pp. 1–17, Jan. 2020.

[4] W. Wu, Z. Peng, D. Wang, L. Liu, and N. Gu, "Anti-disturbance leader–follower synchronization control of marine vessels for underway replenishment based on robust exact differentiators," *Ocean Eng.*, vol. 248, Mar. 2022, Art. no. 110686.

[5] Z. Peng, J. Wang, D. Wang, and Q.-L. Han, "An overview of recent advances in coordinated control of multiple autonomous surface vehicles," *IEEE Trans. Ind. Informat.*, vol. 17, no. 2, pp. 732–745, Feb. 2021.

[6] X. Jin, "Fault tolerant finite-time leader–follower formation control for autonomous surface vessels with LOS range and angle constraints," *Automatica*, vol. 68, pp. 228–236, Jun. 2016.

[7] S.-L. Dai, S. He, Y. Ma, and C. Yuan, "Cooperative learning-based formation control of autonomous marine surface vessels with prescribed performance," *IEEE Trans. Syst., Man, Cybern., Syst.*, vol. 52, no. 4, pp. 2565–2577, Apr. 2022.

[8] B. S. Park and S. J. Yoo, "An error transformation approach for connectivity-preserving and collision-avoiding formation tracking of networked uncertain underactuated surface vessels," *IEEE Trans. Cybern.*, vol. 49, no. 8, pp. 2955–2966, Aug. 2019.

[9] B. S. Park and S. J. Yoo, "Connectivity-maintaining and collision-avoiding performance function approach for robust leader–follower formation control of multiple uncertain underactuated surface vessels," *Automatica*, vol. 127, May 2021, Art. no. 109501.

[10] S. He, M. Wang, S.-L. Dai, and F. Luo, "Leader–follower formation control of USVs with prescribed performance and collision avoidance," *IEEE Trans. Ind. Informat.*, vol. 15, no. 1, pp. 572–581, Jan. 2019.

[11] S.-L. Dai, S. He, H. Cai, and C. Yang, "Adaptive leader–follower formation control of underactuated surface vehicles with guaranteed performance," *IEEE Trans. Syst., Man, Cybern. Syst.*, vol. 52, no. 3, pp. 1997–2008, Mar. 2022.

[12] Z. Peng, N. Gu, Y. Zhang, Y. Liu, D. Wang, and L. Liu, "Path-guided time-varying formation control with collision avoidance and connectivity preservation of under-actuated autonomous surface vehicles subject to unknown input gains," *Ocean Eng.*, vol. 191, Nov. 2019, Art. no. 106501.

[13] Z. Peng, D. Wang, T. Li, and M. Han, "Output-feedback cooperative formation maneuvering of autonomous surface vehicles with connectivity preservation and collision avoidance," *IEEE Trans. Cybern.*, vol. 50, no. 6, pp. 2527–2535, Jun. 2020.

[14] Z. Peng, L. Liu, and J. Wang, "Output-feedback flocking control of multiple autonomous surface vehicles based on data-driven adaptive extended state observers," *IEEE Trans. Cybern.*, vol. 51, no. 9, pp. 4611–4622, Sep. 2021.

[15] N. Gu, D. Wang, Z. Peng, and L. Liu, "Observer-based finite-time control for distributed path maneuvering of underactuated unmanned surface vehicles with collision avoidance and connectivity preservation," *IEEE Trans. Syst., Man, Cybern., Syst.*, vol. 51, no. 8, pp. 5105–5115, Aug. 2021.

[16] G. Lv, Z. Peng, H. Wang, L. Liu, D. Wang, and T. Li, "Extended-state-observer-based distributed model predictive formation control of under-actuated unmanned surface vehicles with collision avoidance," *Ocean Eng.*, vol. 238, Oct. 2021, Art. no. 109587.

[17] K. D. Do, "Synchronization motion tracking control of multiple underactuated ships with collision avoidance," *IEEE Trans. Ind. Electron.*, vol. 63, no. 5, pp. 2976–2989, May 2016.

[18] B. Wang, S. G. Nersesov, and H. Ashrafiuon, "Robust formation control and obstacle avoidance for heterogeneous underactuated surface vessel networks," *IEEE Trans. Control Netw. Syst.*, vol. 9, no. 1, pp. 125–137, Mar. 2022, doi: 10.1109/TCNS.2022.3141022.

[19] J. Li, G. Zhang, C. Liu, and W. Zhang, "COLREGs-constrained adaptive fuzzy event-triggered control for underactuated surface vessels with the actuator failures," *IEEE Trans. Fuzzy Syst.*, vol. 29, no. 12, pp. 3822–3832, Dec. 2021.

[20] L. Liu, D. Wang, Z. Peng, C. L. P. Chen, and T. Li, "Bounded neural network control for target tracking of underactuated autonomous surface vehicles in the presence of uncertain target dynamics," *IEEE Trans. Neural Netw. Learn. Syst.*, vol. 30, no. 4, pp. 1241–1249, Apr. 2019.

[21] Y. Zhang, D. Wang, Y. Yin, and Z. Peng, "Event-triggered distributed coordinated control of networked autonomous surface vehicles subject to fully unknown kinetics via concurrent-learning-based neural predictor," *Ocean Eng.*, vol. 234, Aug. 2021, Art. no. 108966.

[22] L. Liu, D. Wang, Z. Peng, T. Li, and C. L. P. Chen, "Cooperative path following ring-networked under-actuated autonomous surface vehicles: Algorithms and experimental results," *IEEE Trans. Cybern.*, vol. 50, no. 4, pp. 1519–1529, Apr. 2020.

[23] Y.-L. Wang and Q.-L. Han, "Network-based fault detection filter and controller coordinated design for unmanned surface vehicles in network environments," *IEEE Trans. Ind. Informat.*, vol. 12, no. 5, pp. 1753–1765, Oct. 2016.

[24] X. Wang, Z. Fei, H. Gao, and J. Yu, "Integral-based event-triggered fault detection filter design for unmanned surface vehicles," *IEEE Trans. Ind. Informat.*, vol. 15, no. 10, pp. 5626–5636, Oct. 2019.

[25] Y. Zhang, D. Wang, Z. Peng, and T. Li, "Distributed containment maneuvering of uncertain multiagent systems in MIMO strict-feedback form," *IEEE Trans. Syst., Man, Cybern., Syst.*, vol. 51, no. 2, pp. 1354–1364, Feb. 2021.

[26] Y. Zhang, D. Wang, and Z. Peng, "Consensus maneuvering for a class of nonlinear multivehicle systems in strict-feedback form," *IEEE Trans. Cybern.*, vol. 49, no. 5, pp. 1759–1767, May 2018.

[27] L. Qiao and W. Zhang, "Trajectory tracking control of AUVs via adaptive fast nonsingular integral terminal sliding mode control," *IEEE Trans. Ind. Informat.*, vol. 16, no. 2, pp. 1248–1258, Feb. 2020.

[28] L. Qiao and W. Zhang, "Adaptive second-order fast nonsingular terminal sliding mode tracking control for fully actuated autonomous underwater vehicles," *IEEE J. Ocean. Eng.*, vol. 44, no. 2, pp. 363–385, Apr. 2019.

[29] W. Wu, Z. Peng, D. Wang, L. Liu, and Q.-L. Han, "Network-based line-of-sight path tracking of underactuated unmanned surface vehicles with experiment results," *IEEE Trans. Cybern.*, early access, May 25, 2021, doi: 10.1109/TCYB.2021.3074396.

[30] W. Wu, Z. Peng, L. Liu, and D. Wang, "A general safety-certified cooperative control architecture for interconnected intelligent surface vehicles with applications to vessel train," *IEEE Trans. Intell. Veh.*, early access, Apr. 22, 2022, doi: 10.1109/TIV.2022.3168974.

[31] Z. Peng, J. Wang, and D. Wang, "Distributed maneuvering of autonomous surface vehicles based on neurodynamic optimization and fuzzy approximation," *IEEE Trans. Control Syst. Technol.*, vol. 26, no. 3, pp. 1083–1090, May 2018.

[32] L. Liu, D. Wang, Z. Peng, and T. Li, "Modular adaptive control for LOS-based cooperative path maneuvering of multiple underactuated autonomous surface vehicles," *IEEE Trans. Syst., Man, Cybern., Syst.*, vol. 47, no. 7, pp. 1613–1624, Jul. 2017.

[33] T. Yang, N. Sun, and Y. Fang, "Neuroadaptive control for complicated underactuated systems with simultaneous output and velocity constraints exerted on both actuated and unactuated states," *IEEE Trans. Neural Netw. Learn. Syst.*, early access, Oct. 8, 2021, doi: 10.1109/TNNLS.2021.3115960.

[34] T. Yang, H. Chen, N. Sun, and Y. Fang, "Adaptive neural network output feedback control of uncertain underactuated systems with actuated and unactuated state constraints," *IEEE Trans. Syst., Man, Cybern., Syst.*, early access, Dec. 13, 2021, doi: 10.1109/TSMC.2021.3131843.

[35] L. Wang, A. D. Ames, and M. Egerstedt, "Safety barrier certificates for collisions-free multirobot systems," *IEEE Trans. Robot.*, vol. 33, no. 3, pp. 661–674, Jun. 2017.

[36] M. Srinivasan, S. Coogan, and M. Egerstedt, "Control of multi-agent systems with finite time control barrier certificates and temporal logic," in *Proc. IEEE Conf. Decis. Control (CDC)*, 2018, pp. 1991–1996.

[37] T. I. Fossen, *Handbook of Marine Craft Hydrodynamics and Motion Control*. Hoboken, NJ, USA: Wiley, 2011.

[38] B.-Z. Guo, Z.-H. Wu, and H.-C. Zhou, "Active disturbance rejection control approach to output-feedback stabilization of a class of uncertain nonlinear systems subject to stochastic disturbance," *IEEE Trans. Autom. Control*, vol. 61, no. 6, pp. 1613–1618, Jun. 2016.

[39] Z. Peng, J. Wang, and D. Wang, "Distributed containment maneuvering of multiple marine vessels via neurodynamics-based output feedback," *IEEE Trans. Ind. Electron.*, vol. 64, no. 5, pp. 3831–3839, May 2017.

[40] Z.-L. Zhao and B.-Z. Guo, "Extended state observer for uncertain lower triangular nonlinear systems," *Syst. Control Lett.*, vol. 85, pp. 100–108, Nov. 2015.

[41] N. Gu, D. Wang, Z. Peng, J. Wang, and Q.-L. Han, "Disturbance observers and extended state observers for marine vehicles: A survey," *Control Eng. Pract.*, vol. 123, Jun. 2022, Art. no. 105158.

[42] A. Chalanga, S. Kamal, L. M. Fridman, B. Bandyopadhyay, and J. A. Moreno, "Implementation of super-twisting control: Super-twisting and higher order sliding-mode observer-based approaches," *IEEE Trans. Ind. Electron.*, vol. 63, no. 6, pp. 3677–3685, Jun. 2016.

[43] E. Cruz-Zavala and J. A. Moreno, "Levant's arbitrary-order exact differentiator: A Lyapunov approach," *IEEE Trans. Autom. Control*, vol. 64, no. 7, pp. 3034–3039, Jul. 2019.

[44] G. Li, Z. Yan, and J. Wang, "A one-layer recurrent neural network for constrained nonsmooth invex optimization," *Neural Netw.*, vol. 50, pp. 79–89, Feb. 2014.

[45] M. Benzaoui, H. Chekireb, M. Tadjine, and A. Boulkroune, "Trajectory tracking with obstacle avoidance of redundant manipulator based on fuzzy inference systems," *Neurocomputing*, vol. 196, pp. 23–30, Jul. 2016.

[46] Y. Hong, J. Huang, and Y. Xu, "On an output feedback finite-time stabilization problem," *IEEE Trans. Autom. Control*, vol. 46, no. 2, pp. 305–309, Feb. 2001.

[47] R. Skjetne, T. I. Fossen, and P. V. Kokotović, "Adaptive maneuvering, with experiments, for a model ship in a marine control laboratory," *Automatica*, vol. 41, no. 2, pp. 289–298, Feb. 2005.
[48] D. Roetenberg, H. J. Luinge, C. T. M. Baten, and P. H. Veltink, "Compensation of magnetic disturbances improves inertial and magnetic sensing of human body segment orientation," *IEEE Trans. Neural Syst. Rehabil. Eng.*, vol. 13, no. 3, pp. 395–405, Sep. 2005.

Wentao Wu (Student Member, IEEE) received the B.E. degree in electrical engineering and automation from the Harbin University of Science and Technology, Harbin, China, in 2018, and the M.E. degree in electrical engineering from Dalian Maritime University, Dalian, China, in 2021. He is currently pursuing the Ph.D. degree in electronic information with Shanghai Jiao Tong University, Shanghai, China.

He is currently conducting academic exchanges with SJTU Sanya Yazhou Bay Institute of Deepsea Science and Technology, Sanya, China. His current research interests include unmanned surface vehicles, formation control, safety control, and prescribed performance control.

Yibo Zhang (Member, IEEE) received the B.E. degree in marine electronic and electrical engineering and the Ph.D. degree in marine electrical engineering from Dalian Maritime University, Dalian, China, in 2014 and 2021, respectively.

He is a Postdoctoral Fellow with the Department of Automation, Shanghai Jiao Tong University, Shanghai, China. His current research interests include cooperative control and intelligent control of multiagent systems and multiple marine vehicles.

Weidong Zhang (Senior Member, IEEE) received the B.S. degree in measurement technology and instruments, the M.S. degree in applied electronic technology, and the Ph.D. degree in control theory and its application from Zhejiang University, Hangzhou, China, in 1990, 1993, and 1996, respectively.

He worked as a Postdoctoral Fellow with Shanghai Jiaotong University, Shanghai, China. He joined Shanghai Jiaotong University as an Associate Professor in 1998 and has been a Full Professor since 1999. From 2003 to 2004, he worked with the University of Stuttgart, Stuttgart, Germany, as an Alexander von Humboldt Fellow. He is currently the Director of the Engineering Research Center of Marine Automation, Shanghai Municipal Education Commission, Shanghai, and the Director of Marine Intelligent System Engineering Research Center, Ministry of Education, China. He is the author of 265 SCI papers and 1 book, and holds 72 patents. His research interests include control theory and machine learning theory and their applications in industry and autonomous systems.

Prof. Zhang is a recipient of the National Science Fund for Distinguished Young Scholars, China, and the Cheung Kong Scholar, Ministry of Education, China.

Wei Xie (Member, IEEE) received the M.Sc. degree in electromechanical engineering and the Ph.D. degree in electrical and computer engineering from the University of Macau, Macau, China, in 2016 and 2021, respectively.

From 2017 to 2018, he was a Visiting Scholar with the Institute for Systems and Robotics, Laboratory for Robotics and Engineering Systems, Instituto Superior Técnico, Universidade de Lisboa, Lisboa, Portugal. He is currently an Assistant Professor with the Department of Automation, Shanghai Jiao Tong University, Shanghai, China. His research interests include nonlinear control of marine and aerial vehicles and coordinated control of multivehicle systems.